Available online at www.sciencedirect.com
ScienceDirect
Comput. Methods Appl. Mech. Engrg. 410 (2023) 115989
Computer methods in applied mechanics and engineering
www.elsevier.com/locate/cma

Coupling an SPH-based solver with an FEA structural solver to simulate free surface flows interacting with flexible structures

I. Martínez-Estévez[a,*], B. Tagliafierro[b], J. El Rahi[c], J.M. Domínguez[a], A.J.C. Crespo[a], P. Troch[c], M. Gómez-Gesteira[a]

[a] *Environmental Physics Laboratory, CIM-UVIGO, Universidade de Vigo, Spain*
[b] *Laboratori d'Enginyeria Marítima, Universitat Politècnica de Catalunya - BarcelonaTech (UPC) Barcelona, Spain*
[c] *Department of Civil Engineering, Ghent University, Belgium*

Received 9 December 2022; received in revised form 23 February 2023; accepted 3 March 2023
Available online xxxx

Abstract

This work proposes a two-way coupling between a Smoothed Particle Hydrodynamics (SPH) model-based named DualSPHysics and a Finite Element Analysis (FEA) method to solve fluid–structure interaction (FSI). Aiming at having a computationally efficient solution via spatial adjustable resolutions for the two phases, the SPH-FEA coupling herein presented implements the Euler–Bernoulli beam model, based on a simplified model that incorporates axial and flexural deformations, to introduce a solid solver in the DualSPHysics framework. This approach is particularly functional and very precise for slender beam elements undergoing large displacements, and large deformations can also be experienced by the structural elements due to the non-linear FEA implementation via a co-rotational formulation. In this two-way coupling, the structure is discretised in the SPH domain using boundary particles on which the forces exerted by fluid phases are computed. Such forces are passed over to the FEA structural solver that updates the beam shape and, finally, the particle positions are subsequently reshuffled to represent the deformed shape at each time step. The SPH-FEA coupling is validated against four reference cases, which prove the model to be as accurate as other approaches presented in literature.

Keywords: FSI; SPH; FEA; Euler–Bernoulli; DualSPHysics; Project Chrono

1. Introduction

Multiphysics simulations are now becoming mainstream for industry in many application fields, one of which is fluid–structure interaction (FSI) [1]. According to the investigated effect, different classes of problems can be identified under the FSI, in which the physics may strongly differ and whose coupled effects are not negligible. FSI refers to aeroelastic or hydroelastic problems characterised by strong interaction between fluid phases and flexible structures that combined lead to deformations that, in turn, dynamically influence the response of the other medium [2,3]. Other common cases in which FSI becomes relevant are either when structures are extremely *compliant* and so, they closely follow the fluid dynamics and experience large deformations. Another common case is when

* Corresponding author.
E-mail address: ivan.martinez.estevez@uvigo.es (I. Martínez-Estévez).

https://doi.org/10.1016/j.cma.2023.115989

free-surface flows impact deformable structures with sudden changes in pressure, often resulting in portions of fluid being scattered throughout. Relevant examples here come from the simulation of biological systems [4] and impulsive loads on structures [5]. Whatever the instance, the evolution of the fluid and the deformation of the structure should be taken into account seamlessly to preserve the veracity of the numerical prediction.

Traditionally, FSI problems were addressed through mesh-based methods, often considering a partitioned approach and thus, using appropriate Finite Element Methods (FEM) to treat the fluid and the structure separately [6]. However, the fluid mesh should follow the movement of the solid, making the use of remeshing tools essential. Computational costs and convergence issues have led to consider meshless approaches for the fluid phase. Lagrangian particle methods appear to be particularly advantageous for investigating FSI problems due to their meshless nature, which easily allows large deformations and tracking interfaces between the different phases with precision [7]. As the Smoothed Particle Hydrodynamics (SPH) technique is relatively new, SPH-FEM coupling is a recent approach to model FSI [8]: this hybrid method exploits the strengths of both models. Some applications of this methodology are presented in Fourey et al. [9]. A multi-resolution SPH-FEM method for FSI was presented by Chen et al. [10], where the multi-resolution technology can be applied for discretising the fluid and the structure.

Fully Lagrangian approaches have been used for the FSI applications, where both fluids and solids are modelled within the same SPH framework, although employing different techniques. Sun et al. [11] proposed a coupling between a multiphase solver δ-SPH for fluid and a total Lagrangian SPH for the solid solver, which was improved and described in Sun et al. [12]. In addition, a particular mechanical relationship dictating the motion of the rigid bodies such that they mimic flexible elements was described in Capasso et al. [13]. A GPU implementation was presented in O'Connor and Rogers [14], proposing a unified SPH framework for FSI applications. Ren et al. [15] described and validated a fully SPH-based solver to study complex fluid motion with high non-linearity against flexible structures. Other approaches coupled SPH with Discrete Element Method (DEM) such as the one presented in Nasar et al. [16].

One example is the coupled Enhanced Incompressible SPH (ISPH) fluid solver with an SPH-based solid solver presented in Khayyer et al. [17], which provides full validation of the SPH-based solid solver. Similarly, Morikawa and Asai [18] presented a two-way coupling between an Explicit Incompressible SPH (EISPH) fluid solver and an SPH solid solver to deal with FSI problems.

As suggested by the available literature, the use of the SPH method to deal with FSI problems has been growing large and progressing at a very fast pace (see [7]). However, it is well known that particle-based methods, at least when considered in their primordial implementations [19] with a traditional SPH gradient formulation, have to deal with high-frequency non-physical noise pressure. The SPH methods that are influenced by this problem are the so-called weakly compressible SPH (WCSPH), in which an equation of state is solved to obtain the pressure, usually with a stiff relationship that bounds pressure and density fields [20]. A great deal of research has been carried out to face this issue, and the very first algorithm is known as artificial viscosity [21]. One of the most widely accepted pressure enhancers defines a numerical artefact to smooth the density field and it was presented in Antuono et al. [22], lately extended further by Khayyer et al. [23]. As a matter of fact, small particle oscillations do not jeopardise the overall quality of the numerical method as a whole, but it can nonetheless be an issue when an SPH-based solver is embedded in so-called weak coupling schemes with other solvers: this is relevant to FSI applications. Meringolo et al. [24] investigated the limitations of the WCSPH method and provided a filter to mitigate the acoustic noise. On the other hand, other approaches based on SPH, like the ISPH aforementioned, which base the solution of the pressure field on a projection method [25], are inherently devoid of this problem since fluid incompressibility is enforced and guaranteed by solving a Poisson's equation although it presents other drawbacks [26].

The open-source DualSPHysics [27] code is the SPH-based method used in the present work. This code can be freely downloaded from the website www.dual.sphysics.org. It was developed to simulate free-surface flows and their interaction with fixed and floating structures within an international collaborative work between several universities and research centres. DualSPHysics is a highly parallelised implementation of SPH that allows to exploit the capabilities of both multi-core central processing units (CPUs) and graphics processing units (GPUs) [28]. On the other hand, Project Chrono [29] is a multiphysics simulation engine that can be compiled as a library to be coupled as a third-party application, which handles flexible structures and allows solid–solid body interactions with frictional contacts in very large multibody systems with mechanical constraints, among other multiple functionalities. A first coupling between DualSPHysics and Project Chrono was presented in Canelas et al. [30], where a complete system of mechanical constraints was validated by comparing numerical and experimental results for an oscillating

wave surge converter device. Recently, Martínez-Estévez et al. [31] presented an extension of the first coupling DualSPHysics-Chrono, including new features to deal with solid–solid interaction, where the coupling strategy using a general-purpose communication interface (the so-called DSPHChronoLib) to handle the exchange of data between both solvers is described. Within the field of renewable energy, many successful applications have been presented over the last years with the coupled code [32,33].

A new structured version of the DualSPHysics code coupled to the multiphysics library Project Chrono is presented here. Project Chrono implements a non-linear Finite Element Analysis (FEA) method that can deal with flexible structures. As mentioned before, it also supports collision detection algorithms between rigid and flexible bodies and allows simulating multibody dynamics where mechanical constraints can be applied on the bodies. Therefore, in this work, a two-way coupling SPH-FEA is proposed in order to solve FSI, in which the governing equations to solve fluid are handled by the SPH-based model, whereas the FEA solves the structural dynamics. This novel approach comprises several advantages in comparison with other methods: (i) co-operative framework; (ii) resolution independence; (iii) performance and resource optimisation; and (iv) extended capabilities. Considering the first one, the novel methodology presented in this work preserves the accuracy and robustness of the two solvers employed in a co-operative framework. This is, in fact, one of the main advantages of this coupling since the pros of using a meshless SPH method to solve the fluid (adaptable and accurate) are aggregated to those of using a mesh-based mechanical solver (light and precise). Secondly, this methodology allows the possibility of using distinct spatial resolutions for each model, providing a key distinctive feature: *uncoupled resolutions*. The basis of this concept is that even though both models are synchronised and communicate to each other during the simulation, they solve their own systems separately in different environments and the resolutions employed are independent. Considering the performance, the equations to solve the structure using the FEA module of Project Chrono are less expensive in terms of computational cost than approaches using fully Lagrangian solvers. Finally, the multiphysics library Project Chrono provides a wide range of features that promotes the possibility of including more functionalities and so, to extend the capabilities of the coupled model. One example is the use of frictional contact surfaces in FEA meshes in very large multibody systems, where mechanical constraints can be also defined to restrict the movement of flexible elements.

For this first implementation, the FEA solver is coupled by linking the structural element that describes a linear elastic beam known as the Euler–Bernoulli beam model and restricted to 2D. This implies that the method as such cannot deal with stocky elements due to model limitations or experience out-of-plane deformations as the third dimension is not taken into account. The mentioned model is very convenient to test and validate the general structure of the coupling, including its accuracy, robustness and flexibility, as it is computationally inexpensive, and a range of closed-form solutions can be found for academic cases. Nevertheless, it is expected that the co-simulating environment helps to improve the applicability of the proposed SPH framework to industrial applications to a much greater extent.

The contents of this paper are organised as follows: Section 2 shows the main formulation included in the SPH model; Section 3 presents the FEA method integrated in the multiphysics library; Section 4 describes the coupling procedure between both models; Section 5 shows several benchmarks carried out in order to validate the coupling; and finally, Section 6 draws the conclusions of this work.

2. Smoothed particle hydrodynamics solver

This section introduces the main formulation implemented in the DualSPHysics [27] SPH-based numerical model, the novel approach for the boundary conditions and the time step integrator used in this code.

2.1. SPH principle

SPH is a meshless method that discretises a continuum on a set of particles, in which the equations of fluid dynamics are solved. The physical quantities of each particle are obtained as an interpolation of the quantities of its neighbouring particles. The contribution of their neighbours is computed by using a weighting function or kernel (W), whose area of influence is defined by a smoothing length (h). Then, an integral approximation of any function $F(\boldsymbol{r})$ represents the SPH basis by following:

$$F(\boldsymbol{r}) = \int F(\boldsymbol{r}') W(\boldsymbol{r} - \boldsymbol{r}', h)\, d\boldsymbol{r}' \tag{1}$$

being $\boldsymbol{r}$ the position of the point where the function is computed and $\boldsymbol{r}'$ is the position at each time step. Thus, the function F is approximated, in discrete form, by the interpolation of the contribution of all particles belonging to the compact support of the kernel function, following:

$$F\left(\boldsymbol{r}_a\right) \approx \sum_b F\left(\boldsymbol{r}_b\right) \frac{m_b}{\rho_b} W\left(\boldsymbol{r}_a - \boldsymbol{r}_b, h\right) \tag{2}$$

where the subscripts a and b refer to the target particle and the neighbouring particle, respectively, m is the mass and ρ is the density. On the other hand, the weighting function $W(\boldsymbol{r}, h)$, chosen in this work, is the Quintic Wendland kernel [34] that is defined as:

$$W\left(q\right) = \alpha_D \left(1 - \frac{q}{2}\right)^4 \left(2q + 1\right), 0 \leq q \leq 2 \tag{3}$$

being $q = r_{ab}/h$ the non-dimensional distance between particles, r_{ab} is the distance between particles a and b, and α_D is set to $10/7\pi h^2$ in two-dimensional space (2-D).

Note that in DualSPHysics, particles are initially created at the same initial spacing (dp). This spacing is used to define the smoothing length of the simulations. In this work, the smoothing length is $h = 1.2dp$, so that the kernel interaction $2h$ distance is $2.4dp$.

2.2. Governing equations

The discrete form of the Navier–Stokes (N–S) equations is used to govern the motion of the particles in a fluid dynamics system. The momentum equation in Lagrangian form can be written as:

$$\frac{d\boldsymbol{v}_a}{dt} = -\sum_b m_b \left(\frac{p_b + p_a}{\rho_b \rho_a}\right) \nabla_a W_{ab} + \boldsymbol{\Gamma}_a + \boldsymbol{g}, \tag{4}$$

$$\boldsymbol{\Gamma}_a = \sum_b m_b \frac{4\upsilon_0 \boldsymbol{r}_{ab} \cdot \nabla_a W_{ab}}{\left(\rho_a + \rho_b\right)\left(r_{ab}^2 + 0.01h^2\right)} \boldsymbol{v}_{ab} + \sum_b m_b \left(\frac{\tau_a^{ij} + \tau_b^{ij}}{\rho_b \rho_a}\right) \nabla^i W_{ab} \tag{5}$$

where t is the simulation time, $\boldsymbol{v}$ is the velocity, p is the pressure, $\boldsymbol{g}$ is the gravity acceleration and W_{ab} is the kernel function. The dissipation treatment ($\boldsymbol{\Gamma}_a$) is included to the momentum equation, which uses a laminar viscosity (first term) approximated by Lo and Shao [35], and a sub-particle scale model (SPS) (second term) described by Dalrymple and Rogers [36] in which a Favre averaging in a weakly compressible approach is used. The term υ_0 denotes the kinematic viscosity (set to 10^{-6} m^2/s) of the fluid and τ is the SPS stress tensor in Einstein notation in coordinate directions i and j according to:

$$\tau^{ij} = \overline{\upsilon^i \upsilon^j} - \overline{\upsilon^i}\ \overline{\upsilon^j} \tag{6}$$

modelled by an eddy viscosity closure as:

$$\frac{\tau^{ij}}{\rho} = 2\upsilon_{SPS}\left(S^{ij} - \frac{1}{3}S^{ii}\delta^{ij}\right) - \frac{2}{3}C_L \Delta^2 \delta^{ij} \left|S^{ij}\right|^2 \tag{7}$$

being $\upsilon_{SPS} = [C_{SM}\Delta]^2 |S^{ij}|^2$ the turbulent eddy viscosity, $C_{SM} = 0.12$ is the Smagorinsky's constant, $C_L = 0.0066$, Δ is the initial particle spacing and $|S^{ij}| = 1/2(2S^{ij}S^{ij})^{1/2}$, and S^{ij} is an element of the SPS strain tensor. Details of the implementation can be found in the reference paper Domínguez et al. [27].

On the other hand, the continuity equation in discrete form can be expressed following:

$$\frac{d\rho_a}{dt} = \sum_b m_b \boldsymbol{v}_{ab} \cdot \nabla_a W_{ab} + D, \tag{8}$$

$$D = 2\delta h c_s \sum_b \left(\rho_{ba}^T - \rho_{ab}^H\right) \frac{\boldsymbol{r}_{ab} \cdot \nabla_a W_{ab}}{r_{ab}^2} \frac{m_b}{\rho_b} \tag{9}$$

Here, the density diffusion term (D) is added to the continuity equation to reduce fluctuations in the density field, following the formulation presented in Fourtakas et al. [37], in which superscripts T and H represent the total and hydrostatic component of the density, respectively. The approach employed for the density diffusion treatment in this work is based on the formulation presented in Molteni and Colagrossi [38], but introducing a correction for

which the dynamic density is replaced with the total density (ρ^T). The term c_s is the numerical speed of sound and being δ the coefficient that controls this diffusion term (set to 0.1). Thus, for a weakly compressible fluid, the hydrostatic pressure difference of particles a and b is computed as:

$$p_{ab}^H = \rho_0 g z_{ab} \tag{10}$$

where z_{ab} is the vertical distance between particles a and b. Despite the use of a formulation based on the one described in Molteni and Colagrossi [38] carries some inconsistencies near the wall boundaries, the use of total density improves the behaviour of the pressure near the wall boundaries as it was demonstrated by Fourtakas et al. [37]. It should be noted that in Antuono et al. [39] a general approach is described, known as δ-SPH, which ensures the consistency of the density fluid at free surface, but it implies the computation of a normalised density gradient, whereas in Fourtakas et al. [37] it is not needed to perform that extra calculation and their approach works accurately for gravity-dominated flows with significantly lower computational cost.

DualSPHysics code includes a weakly compressible SPH formulation to solve the fluid pressure, and therefore, the pressure (p) is obtained from the particle density (ρ) by using the following equation of state:

$$p = \frac{c_s^2 \rho_0}{\gamma_p} \left[\left(\frac{\rho}{\rho_0} \right)^{\gamma_p} - 1 \right] \tag{11}$$

where $\rho_0 = 1000$ kg/m^3 is the reference density of the fluid and $\gamma_p = 7$ is the polytropic constant.

2.3. Boundary conditions

DualSPHysics implements the modified Dynamic Boundary Conditions (DBC) method (the so-called mDBC) proposed by English et al. [40], which is a modification of the original DBC method formerly presented in Crespo et al. [41] and originally conceived by [42]. The boundary particle arrangement within the mDBC implementation is done following the same strategy of the DBC (see [41]). However, a boundary interface is created some distance from the innermost layer of boundary particles, usually at $dp/2$ for simple shapes. An example of this novel method is depicted in Fig. 1, in which the boundary interface is represented with a black line. A ghost node (cross) is created in the fluid domain for each boundary particle (the so-called target boundary particle in Fig. 1), following the procedure proposed by Marrone et al. [43]. Normal vectors (arrows) are defined from the boundary particles to the boundary interface, pointing in the fluid domain direction. Then, the ghost node is projected according to its normal vector. When flat boundaries are modelled, the ghost node is mirrored across the boundary interface; otherwise for boundary particles placed in a corner, the ghost node is mirrored through this corner into the fluid domain.

Following this novel methodology, boundary particles obtain the fluid properties computed through a corrected SPH approximation at the ghost node, where the density field is evaluated considering the procedure proposed by Liu and Liu [44]. Then, the density of the ghost node (ρ_g) is obtained as:

$$\rho_g = \frac{\sum_j \rho_j W_{gj} \frac{m_j}{\rho_j}}{\sum_j W_{gj} \frac{m_j}{\rho_j}} \tag{12}$$

When the ghost node incorporates the new density value, the density of the boundary particle (ρ_b) is obtained by following:

$$\rho_b = \rho_g + \left(r_b - r_g \right) \cdot \left[\partial_x \rho_g ; \partial_y \rho_g ; \partial_z \rho_g \right] \tag{13}$$

where r_b is the position of the boundary particle, r_g is the position of the associated ghost node, and $[\partial_x \rho_g ; \partial_y \rho_g ; \partial_z \rho_g]$ is the gradient computed at the ghost node considering a first-order consistent SPH interpolation [44]. This approach offers a more accurate and smoother pressure field. More details can be found in [40].

In DualSPHysics, the basic equations of rigid body dynamics are implemented in order to simulate the motion of fluid-driven objects [45]. The motion of a fluid-driven object is derived by considering its interaction with fluid and its own weight. In this SPH code, the rigid bodies are considered as a fluid-driven object composed by boundary particles k. Thus, the net force exerted by the fluid is computed on each boundary particle of the object according

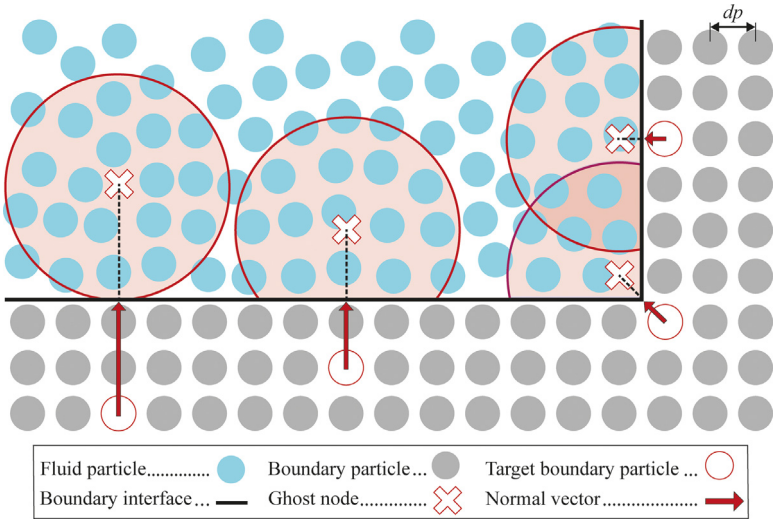

Fig. 1. Projection of ghost nodes when the mDBC method is applied.

to the sum of the contributions of all surrounding fluid particles. Therefore, each boundary particle k experiences a force per unit mass given by:

$$\boldsymbol{f}_k = \sum_a \boldsymbol{f}_{ka} \tag{14}$$

where $\boldsymbol{f}_{ka}$ is the force per unit mass exerted by the fluid particle a on the boundary particle k.

2.4. Time integrator scheme

DualSPHysics implements the symplectic position Verlet (the so-called Symplectic) time integrator scheme [46], which is an explicit and second-order accurate in time scheme. For brevity, the governing equations can be written as:

$$\frac{d\boldsymbol{v}_a}{dt} = \boldsymbol{f}_a; \ \frac{d\rho_a}{dt} = R_a; \ \frac{d\boldsymbol{r}_a}{dt} = \boldsymbol{v}_a \tag{15}$$

When viscous density forces and density evolution are present in DualSPHysics, the velocity is required at the $(n + 1/2)$ step. Therefore, a velocity Verlet half step is used to compute the required velocity for the acceleration and density evolution for $\boldsymbol{f}(\boldsymbol{r}_{n+1/2})$ and $R(\boldsymbol{r}_{n+1/2})$, respectively. Then, the scheme implemented in DualSPHysics is given by:

$$\begin{aligned}
\boldsymbol{r}_a^{n+1/2} &= \boldsymbol{r}_a^n + \tfrac{\Delta t_{SPH}}{2}\boldsymbol{v}_a^n, \\
\boldsymbol{v}_a^{n+1/2} &= \boldsymbol{v}_a^n + \tfrac{\Delta t_{SPH}}{2}\boldsymbol{f}_a^n, \\
\boldsymbol{v}_a^{n+1} &= \boldsymbol{v}_a^n + \Delta t_{SPH}\boldsymbol{f}_a^{n+1/2}, \\
\boldsymbol{r}_a^{n+1} &= \boldsymbol{v}_a^n + \Delta t_{SPH}\left(\tfrac{\boldsymbol{v}_a^{n+1}+\boldsymbol{v}_a^n}{2}\right)
\end{aligned} \tag{16}$$

Finally, the density evolution is computed according the half time step of the symplectic position Verlet scheme by following [47], whose form is given by:

$$\begin{aligned}
\rho_a^{n+1/2} &= \rho_a^n + \tfrac{\Delta t_{SPH}}{2}R_a^n, \\
\rho_a^{n+1} &= \rho_a^n + \tfrac{2-\varepsilon_a^{n+1/2}}{2+\varepsilon_a^{n+1/2}}
\end{aligned} \tag{17}$$

being $\varepsilon_a^{n+1/2} = -\left(\frac{R_a^{n+1/2}}{\rho_a^{n+1/2}}\right)\Delta t_{SPH}$

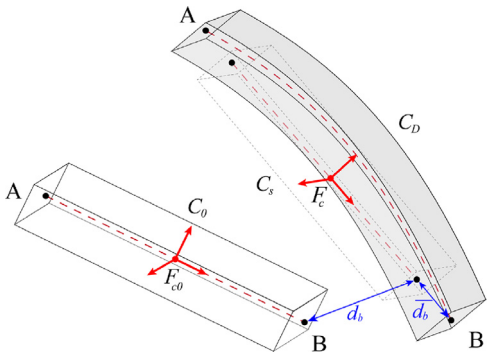

Fig. 2. Concept of the co-rotational formulation implemented in Project Chrono (inspired by [52]).

DualSPHysics implements a variable time step (Δt_{SPH}) that is controlled by a CFL (Courant–Friedrich–Lewy) condition, in which the force term (Δt_f) and the viscous diffusion term (Δt_{cv}) follow [48], and are defined as:

$$\Delta t_f = \min_a \left(\sqrt{h / \left| \frac{d\boldsymbol{v}_a}{dt} \right|} \right); \quad \Delta t_{cv} = \min_a \frac{h}{c_s + \max_b \frac{|h\boldsymbol{v}_a \cdot \boldsymbol{r}_a|}{r_{ab}^2 + 0.01^2}} \tag{18}$$

So, the final value of the integrator time step is given by:

$$\Delta t_{SPH} = 0.2 \min \left(\Delta t_f, \Delta t_{cv} \right) \tag{19}$$

Details on the implementation of the time integrator scheme and the variable time step in DualSPHysics are given in [27].

3. FEA structural solver

The core module of Project Chrono (*Chrono::Engine*) supports the modelling of non-linear Finite Element Analysis (FEA) to solve flexible multibody systems [29]. In this work, the flexible elements are solved with the co-rotational (CR) approach, whose theory can be seen for instance in Belytschko and Glaum [49], and Felippa and Haugen [50]. The CR concept is a Finite Element Method (FEM) that allows large displacements and rotations, but strains and deformations must be small when linear systems are considered. However, Project Chrono implements a non-linear FEA via CR formulation where large deformations are allowed in structural elements, such as the classical three-dimensional (3-D) Euler–Bernoulli beam, based on the work presented in Rankin and Nour-Omid [51].

In this CR implementation, a floating coordinate system (F_c) is considered to follow the deformed shape of the elements, where a reference configuration (C_0) of the element is used to compute the deformed state (C_D) from a superposition between C_0 to the so-called *floating* or *shadow configuration* (C_s). In addition, a local small-strain deformation is included from C_s to C_D [52]. Fig. 2 depicts the concept of the CR formulation as implemented in this multiphysics library. Assuming that the flexible elements are discretised as 3-D beams composed of two end-nodes (denoted by A and B) and six degrees of freedom (DOFs) at each node, the initial frame position is placed in the midpoint of the two nodes.

Project Chrono computes the global stiffness matrix ($\boldsymbol{K_e}$) and the global force ($\boldsymbol{f_e}$) vector of the beam element from the local components $\overline{\boldsymbol{K}_e}$ and $\overline{\boldsymbol{f}_e}$, which represent the local stiffness matrix and the local force vector, respectively. Note that the overlined terms indicate quantity in the local reference system. First of all, the local displacement ($\overline{\boldsymbol{d}}$) is defined by considering the components that can produce a deformation in the beam:

$$\overline{\boldsymbol{d}} = \left(\overline{\boldsymbol{d}}_A, \overline{\boldsymbol{\theta}}_A, \overline{\boldsymbol{d}}_B, \overline{\boldsymbol{\theta}}_B \right) \tag{20}$$

where $\overline{\boldsymbol{d}}_A$ and $\overline{\boldsymbol{d}}_B$ are the local displacements, and $\overline{\boldsymbol{\theta}}_A$ and $\overline{\boldsymbol{\theta}}_B$ are the local finite rotations referred to the end nodes of the beam. Details of this formulation are given in Crisfield et al. [53], and in Tasora and Masarati [52].

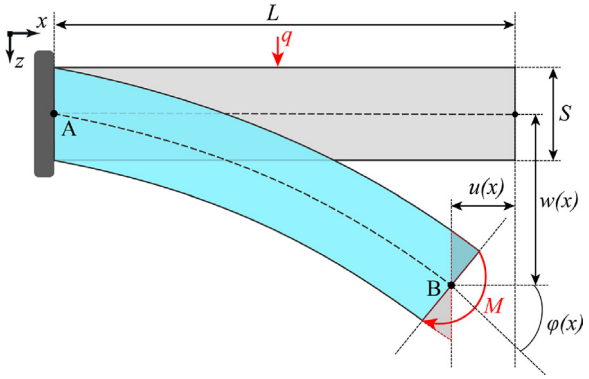

Fig. 3. Schematic of the Euler–Bernoulli beam theory in 2-D.

Once $\overline{\boldsymbol{d}}$ is obtained, the local nodal forces ($\overline{\boldsymbol{f}_{in}}$) are computed from the local stiffness matrix and the local displacements using:

$$\overline{\boldsymbol{f}_{in}} = \overline{\boldsymbol{K}_{\boldsymbol{e}}}\,\overline{\boldsymbol{d}} \tag{21}$$

Finally, $\overline{\boldsymbol{f}_{in}}$ and $\overline{\boldsymbol{K}_{\boldsymbol{e}}}$ are transformed from the local system into global coordinates following the approach presented in [50] and in [52]. The method can be applied to beam elements composed of two nodes and 6-DOFs such as the classical Euler–Bernoulli beams available in Project Chrono.

3.1. Euler–Bernoulli beam

The classical Euler–Bernoulli beam theory is used to provide a simplified framework for anticipating the response of structural elements. As such, finite elements can be modelled and solved under the Euler–Bernoulli theory to compute the deformation of beams considering their internal stress (see for instance [54]). A 3-D beam is usually identified as a geometrical structure in which one of its dimensions is much larger than the other two, being the largest dimension considered the axis of the beam and the cross-section normal to the axis. Fig. 3 shows a schematic of a Euler–Bernoulli beam, in this case, represented in 2-D, being A the fixed end-node and B the free-end node.

In this work, the main kinematic formulae about the Euler–Bernoulli beams are presented in the following:

$$w = w\,(x) \tag{22}$$

$$\varphi\,(x) = -\frac{dw\,(x)}{dx} \tag{23}$$

where x is the axis direction of the beam, w is the displacement orthogonal to the axis or axial displacement, and φ is the rotation or sectional displacement with respect to the axial direction of the beam. Eq. (23) implicitly contains the condition that uniquely characterises the Euler–Bernoulli approach in which the kinematic of each cross section strictly forms a 90-degree angle with the deflected shape of the beam.

The governing equation to solve the deflection of a homogeneous (i.e., same material) and uniform (i.e., same cross section within A and B) beam is defined as:

$$q\,(x) = -\varphi\,(x)\left(EI\frac{d\varphi\,(x)}{dx}\right) \tag{24}$$

where $q(x)$ is the transversal load, E the Young's Modulus, and I the second moment of the inertia of the cross-section, being the product EI called flexural rigidity.

Assuming the structure is modelled as a co-rotated Euler–Bernoulli beam, the translation $u(x)$ of the element depends on Eq. (23), which contains the displacements and rotations of the end nodes. The state is used to compute the deflection φ along the axis and then, when the deflection is known, the bending moment function (M) can be evaluated with the following equation:

$$M\,(x) = -EI\left(\frac{d\varphi\,(x)}{dx}\right) \tag{25}$$

The normal stress along the cross section (σ_{xx}) induced by bending moment (M) can be evaluated using the Navier's hypothesis [55] that gives:

$$\sigma_{xx}(x) = -\frac{M(x)}{I} y \tag{26}$$

where y is the distance between the point of interest (may not belong to the cross-section) and the beam axis along the height of the cross section. This definition yields a linear relationship between distance from the neutral axis and the considered point.

The Euler–Bernoulli defined as such provides a very advantageous tool that requires little computational overhead and little data transfer. Nevertheless, the model has certainly got limitations, and they generate from the particular conditions in which the theory thrives. In particular, the model cannot accurately capture the kinematic of beams for which shear forces are relevant and can only capture linearly distributed stress patterns. It can nonetheless accurately and reliably proxy slender beams, as it will be shown in Section 5.

3.2. Time integrator scheme

The implicit time integrator Hilber–Hughes–Taylor (HHT) proposed by Hilber et al. [56] is available in Project Chrono. This time integrator scheme is able to deal with structural dynamic systems using a set of second-order Ordinary Differential Equations (ODE). Therefore, the HHT scheme can be used to simulate flexible structures within the FEA approach. This scheme generalises the Newmark's algorithm proposed by Newmark [57] for second-order ODE systems. Details of the implementation of HHT and Newmark's in Project Chrono are given in Negrut et al. [58]. Then, the system using Newmark's algorithm is integrated in time:

$$\boldsymbol{M}\frac{d^2\boldsymbol{q}}{dt^2} + \boldsymbol{C}\frac{d\boldsymbol{q}}{dt} + \boldsymbol{K}\boldsymbol{q} = \boldsymbol{F_e}(t) \tag{27}$$

where $\boldsymbol{M}$, $\boldsymbol{C}$ and $\boldsymbol{K}$ are mass, damping and stiffness matrices, respectively, and $\boldsymbol{F_e}$ is the vector of external forces, which varies in time t, whereas $\boldsymbol{q}$ represents the configuration of the system as a set of generalised coordinates. In this work, $\boldsymbol{F_e}$ constitutes the communication interface that realises the connection with the externally computed loads from the SPH particle interaction. The Newmark's scheme is solved assuming the following integration formulae:

$$\boldsymbol{q}^{n+1} = \boldsymbol{q}^n + \Delta_{Ch}\frac{d\boldsymbol{q}^n}{dt} + \frac{\Delta_{Ch}^2}{2}\left[(1-2\beta)\frac{d^2\boldsymbol{q}^n}{dt^2} + 2\beta\frac{d^2\boldsymbol{q}^{n+1}}{dt^2}\right], \tag{28}$$

$$\frac{d\boldsymbol{q}^{n+1}}{dt} = \frac{d\boldsymbol{q}^n}{dt} + \Delta_{Ch}\left[(1-\gamma)\frac{d^2\boldsymbol{q}^n}{dt^2} + \gamma\frac{d^2\boldsymbol{q}^{n+1}}{dt^2}\right] \tag{29}$$

where the terms β and γ are the parameters to govern the numerical dissipation of the algorithm, which can be defined as:

$$\gamma \geq \frac{1}{2}; \quad \beta \geq \frac{\left(\gamma + \frac{1}{2}\right)^2}{4} \tag{30}$$

Eqs. (28) and (29) are used to discretise the equations of motion (Eq. (27)) at time t^{n+1} by using an integration time step (Δt_{Ch}), and following:

$$\boldsymbol{M}\frac{d^2\boldsymbol{q}^{n+1}}{dt^2} + \boldsymbol{C}\frac{d\boldsymbol{q}^{n+1}}{dt} + \boldsymbol{K}\boldsymbol{q}^{n+1} = \boldsymbol{F_e}\left(t^{n+1}\right) \tag{31}$$

This method becomes second-order accurate when the values $\gamma = 1/2$ and $\beta = 1/4$ are considered. However, it does not introduce any numerical damping in the solution, making it impractical to address problems where high-frequency oscillations can disturb the system's solution [58]. This indeed is the main drawback of the Newmark's family of integrators: they are not able to provide second-order accuracy along with desirable level of numerical damping. Conversely, the HHT method stands out because it overcomes the issue of its predecessor due to it is unconditionally stable, preserves the numerical damping properties, and achieves second-order accuracy [58]. It includes an extra dissipation quotient (so-called α) to Eq. (31), which makes it an optimal and accurate method, if wisely employed, when some numerical damping is required to damp out high-order mode of vibration effects,

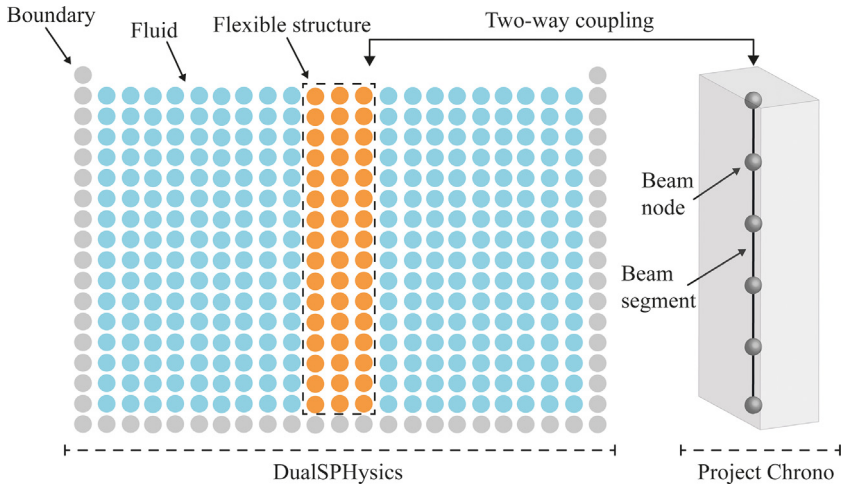

Fig. 4. Discretisation of the domain in DualSPHysics and Project Chrono.

which often arise in flexible structure with high multiplicity of connected elements. The equation of motion for the HHT scheme can be written as:

$$\boldsymbol{M}\frac{d^2\boldsymbol{q}^{n+1}}{dt^2} + (1+\alpha)\,\boldsymbol{C}\frac{d\boldsymbol{q}^{n+1}}{dt} - \alpha\boldsymbol{C}\frac{d\boldsymbol{q}^{n}}{dt} + (1+\alpha)\,\boldsymbol{K}\boldsymbol{q}^{n+1} - \alpha\boldsymbol{K}\boldsymbol{q}^{n} = \boldsymbol{F}_{\boldsymbol{e}}\left(\tilde{t}^{n+1}\right), \tag{32}$$

$$\tilde{t}^{n+1} = t^n + (1+\alpha)\,\Delta_{Ch} \tag{33}$$

where $\alpha \in [-1/3, 0]$ and the parameters to govern the numerical dissipation of HHT algorithm are defined, following [58], by:

$$\gamma = \frac{1}{2} - \alpha; \quad \beta = \frac{(1-\alpha)^2}{4} \tag{34}$$

Therefore, the HHT scheme works as the Newmark's when $\alpha = 0$ (i.e., $\gamma = 1/2$ and $\beta = 1/4$) as it clearly indicates that there is no numerical damping applied and is second order accurate. Otherwise, numerical dissipation is present for $\gamma > 1/2$, and the larger the value of α, the more damping is induced in the numerical solution. In this work, the HHT integrator has been used to solve the structure with $\alpha = 0$ since no dissipation is required for the cases reproduced in the validation section (see in Fourey et al. [9]).

4. SPH-FEA coupling

The novel implementation presented in this manuscript is based on a two-way coupling of the SPH model with the FEA structural solver described in Section 3. The DualSPHysics code solves the fluid–fluid and fluid–solid interactions, and the behaviour of the deformable object is simulated using the FEA structural solver integrated in Project Chrono. The entire domain is described using subsets of particles within the SPH solver, including the flexible structure as a set of boundary particles. On the other hand, within the FEA solver, the structure is built with a set of segments (N) that connects nodes ($N + 1$). The segments are modelled using beam elements under the Euler–Bernoulli formulation (Section 3.1), whereas the beam nodes are 3-D finite element nodes with 6-DOFs. Fig. 4 shows the discretisation of the domain in both models (DualSPHysics and Project Chrono).

DualSPHysics and Project Chrono exchange data to simulate the fluid–elastic structure interactions within a two-way procedure via a communication interface, where DualSPHysics controls the communication making calls to Project Chrono. The data exchange process can be split into two event flows: (i) initial setup; and (ii) time step integration. These events are explained in the following subsections.

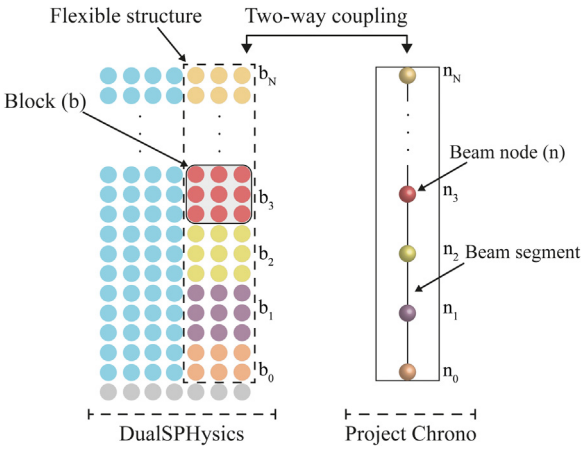

Fig. 5. Initial setup of the flexible structure in DualSPHysics and Project Chrono.

4.1. Initial setup flow

Initially, DualSPHysics transfers to Project Chrono the density of the structure (ρ), number of structure segments (N), damping coefficient (c), Young's Modulus (E), and Poisson's ratio (ν) to model the elastic structure. After that, Project Chrono returns the vector with the initial positions of the nodes ($\boldsymbol{R}_0$). Once the initial setup is completed, the structure is built and discretised in both the SPH and the FEA domains. The SPH solver divides the flexible structure into $N + 1$ blocks. The concept of block represents a set of particles of the structure that will be linked to a FEA beam node. Fig. 5 shows the initial setup where the blocks are identified with b_i and the beam nodes with n_i, being $i \in [0, N]$ the index of the blocks and nodes. The approach followed in this work is such that the SPH solver computes linear forces exerted by the fluid on the blocks and the FEA structural solver simulates the movement and the deformation of the flexible structure by applying those forces on the beam nodes. It should be noted that the model presented here does not account the torsional forces exerted by the fluid since it is focused on 2-D simulations yet, where the torsion of the beam is neglected.

4.2. Time integration flow

In the time step integration flow, both models exchange data in order to solve fluid–structure interaction. Then, the advance of a SPH time step (Δt_{SPH}) is solved, which is repeated until the maximum simulation time is achieved (t_{MAX}). The process of simulating a Δt_{SPH} can be split into three steps: (i) compute the linear forces ($\boldsymbol{F}$) on the structure; (ii) solve the movement of the structure ($\boldsymbol{R}$); and (iii) update the magnitudes of the structure particles. The coupled model presented in this work is based on the coupling strategy presented in Martínez-Estévez et al. [31] by using the general-purpose communication interface DSPHChronoLib to handle the data exchange process between DualSPHysics and Project Chrono. The use of this interface as a link between both solvers facilitates the development tasks since it follows a *low coupling* strategy, which means that new changes or features implemented in either solver would not affect the operation of the other [31]. A complete schematic of the flow events is shown in Fig. 6.

The three steps involved during the simulation are depicted in Fig. 7 and explained here in detail:

(i) DualSPHysics computes the particle interaction by solving the SPH governing equations (4) and (8) considering the fluid–structure interaction and linear ($d\boldsymbol{V}/dt$) and angular ($d\boldsymbol{\Omega}/dt$) accelerations are obtained. The SPH model computes the linear forces on the structure particles by solving the Eq. (14). Then, the linear forces ($\boldsymbol{F}_i$) on each block b_i are computed as the sum of all the forces of the particles belonging to it. Therefore, the vector includes the total force exerted by the fluid on the block b_i. Thus, the forces computed on the block b_i, will be applied on the node n_i.

(ii) DualSPHysics transfers $\boldsymbol{F}_i$ to Project Chrono through DSPHChronoLib. The FEA structural solver applies $\boldsymbol{F}_i$ on its respectively node n_i and solves the movement of the structure. This process usually takes several

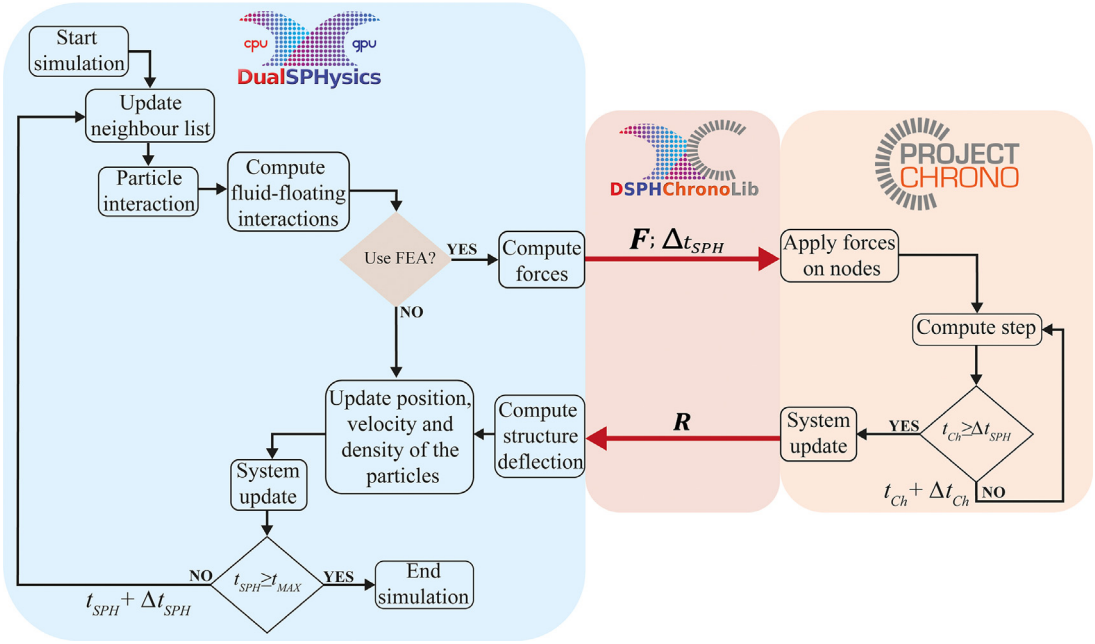

Fig. 6. Scheme of the two-way time step integration flow of the coupled model.

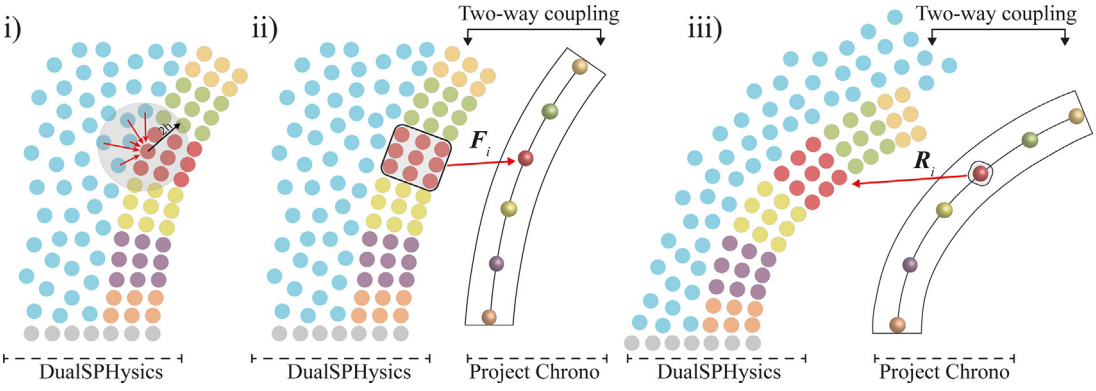

Fig. 7. Main steps during the time step integration of the two-way coupling between DualSPHysics and Project Chrono to solve fluid–structure interactions.

internal integration time steps (Δt_{Ch}), and therefore, it goes on until the loop exit condition is satisfied ($t_{Ch} \geq \Delta t_{SPH}$) and Project Chrono updates the system. The behaviour of the flexible structure is considered to obtain the variable Δt_{SPH} (computed in Eq. (19)) since the velocity of its particles is taken account in Eq. (18). Note that t_{Ch} is not the absolute internal time of the simulation in the multiphysics library, hence it is relative to each Δt_{SPH} that is solved.

(iii) Project Chrono transfers back the node positions ($\boldsymbol{R}_i$) to DualSPHysics through DSPHChronoLib. Then, DualSPHysics computes the deformation of the shape in SPH and updates the position ($\boldsymbol{r}$), velocity ($\boldsymbol{v}$), density (ρ) and pressure (p) of all particles. At this point, the system is ready to be updated and to solve the next time step, if any.

5. Validation cases

The literature revised in the introduction provides examples of benchmark cases useful for accuracy comparison. In this section, four benchmarks are presented in order to validate the proposed coupled model for FSI: (i) freely

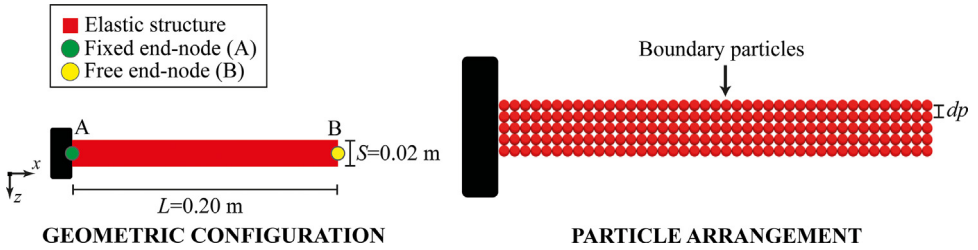

Fig. 8. Geometric configuration and initial particle arrangement of the cantilevered beam for an SPH resolution $dp = S/4$.

oscillating cantilevered beam; (ii) hydrostatic water column on an elastic beam; (iii) breaking water column with an elastic gate; and (iv) breaking water column impacting an elastic obstacle. All the simulations included in this section are carried out on a personal computer with AMD Ryzen 9 5950X CPU and a graphic card NVIDIA RTX A5000. The SPH solver of DualSPHysics is executed on the GPU while Project Chrono is solved on a single-core CPU thread.

5.1. A freely oscillating cantilevered beam

Prior to presenting proper FSI cases, a first benchmark is herein used to ascertain the agreement of the structure solution under dynamic conditions, which allows validating the management of the coupled library by the main code DualSPHysics. The undamped, dynamic response of a cantilevered beam subjected to an initial velocity distribution is compared to an analytical solution that was derived from the theory of thin plates developed by Landau and Lifshitz [59]. Fig. 8 shows the geometry of the cantilevered beam that is composed of two end-nodes (A and B), whose dimensions are length $L = 0.20$ m and thickness $S = 0.02$ m and its elastic material properties are Young's modulus $E = 1.68$ MPa, Poisson's ratio $\nu = 0.40$, and density $\rho = 1000$ kg/m^3. The motion of a freely oscillating plate at its free-end (node B in Fig. 8), described by its middle plane line in a 2-D framework, is given into closed form as:

$$w\,(L,t) = \frac{\psi c_s}{\omega} \cdot \cos\left(\omega t\right) \tag{35}$$

where w is the displacement in the complementary direction to the axis, ψ is a scaling factor (set to 1/100), being $c_s = \sqrt{K/\rho}$ the speed of sound of the material, $K = E/(3(1-2\nu)$ the bulk modulus and ω the circular frequency of oscillation defined as:

$$\omega = k_w^2 \sqrt{\frac{EIT}{12\rho\left(1-\nu^2\right)}} \tag{36}$$

where k_w is the wave number that corresponds to the first mode (i.e., $k_w = 1.875/L$), I is the beam area moment of inertia of the cross section.

The boundary conditions imposed to the beam to realise a clamped-free-end static scheme are:

$$w\,(A) = 0; \quad \frac{\partial w}{\partial x}\,(A) = 0; \quad \frac{\partial^2 w}{\partial x^2}\,(B) = 0; \quad \frac{\partial^3 w}{\partial x^3}\,(B) = 0 \tag{37}$$

whereas an initial velocity field is imposed to the beam's axis as:

$$\frac{\partial w\,(x)}{\partial t} = \psi c_s \frac{f\,(x)}{f\,(x=L)} \tag{38}$$

in which $f\,(x)$ is defined according to the following function:

$$\begin{aligned} f\,(x) = {} & (\cos k_w L + \cosh k_w L)\,(\cosh k_w x - \cos k_w L) \\ & + (\sin k_w L - \sinh k_w L)\,(\sinh k_w x - \sin k_w x) \end{aligned} \tag{39}$$

Note that the Neumann boundary conditions are enforced at (internal) node level, meaning that the vertical velocity profile is discretised according to the node position along the axis and so this approach asymptotically tends to the continuous distribution when the number of nodes (segments) increases.

Table 1
Performance of the freely oscillating cantilevered beam case for $dp = S/4$.

dp	Structure particles	Fluid particles	Segments (N)	SPH steps	DualSPHysics runtime [s]	Chrono runtime [s]	Total runtime [s]	% Chrono
$S/4$	205	–	10	44 195	104	30	134	22
$S/4$	205	–	20	44 195	106	33	139	24
$S/4$	205	–	30	44 195	108	42	150	28

Fig. 8 visualises the initial solid layout for the beam and the initial particle setup corresponding to the initial interparticle distance $dp = S/4$. According to the coupling procedure presented in Section 4, regardless of the fluid presence, the initial value of dp must guarantee a minimum width of one particle per segment so that there is consistency between the geometric beam configuration in both spaces. However, this test case does not involve the solution of any fluid phase and the structure is completely resolved within the Project Chrono subroutine thus giving no relevance to the particle discretisation.

It is important to underline that to compare the results of a Euler–Bernoulli beam model to plate theory's, a correction must be implemented to account for the different hypotheses on which the two theories develop to predict the steady-state solution for thin elements. In the first place, the slenderness of the beam herein considered (i.e., $\propto L/S$) classifies as slender, and for which the Euler–Bernoulli theory should be providing good estimation of the overall kinematics. However, the same geometric configuration gives rise to two different flexural rigidities that differ for a constant value introduced by further deformability of the planar model, as it was proposed in [60] and recently demonstrated and validated in [13]. The computation of the correction follows:

$$\hat{E} = \frac{E}{1-\nu^2} \tag{40}$$

where $\hat{E}$ represents the corrected value to be used to define the axial and flexural stiffness that are passed to the structural solver. Using the value defined by means of Eq. (40) allows to use the solution of Eq. (35) as reference.

To assess the accuracy and precision of the structural model, three simulations with $N = 10$, 20, and 30 segments are respectively run, and the results are collected in Fig. 9 in terms of dimensionless tip deflection in time (node B) using the theoretical maximum motion amplitude $(\psi c_s)/\omega = 0.0025$ m (see Eq. (35)). Note that with the maximum deflection being small in comparison to the beam length, the validity of the theoretical solution obtained using the linear theory is ensured. The beam tip deflection matches the theoretical target for each case, showing hardly any dispersion among the considered FEM resolutions. The agreement is quantified here measuring the L_1 error for the amplitude and the period when $N = 30$ is used. A proper reproduction of the displacement function is shown, with a frequency error of about 3% ($\omega_{theory} = 20.82$ rad/s against $\omega_{num} = 20.27$ rad/s) an overall error on the amplitude around 1.5%, which specifically accounts for an almost 2%-error for the positive peaks and a 0.2% for the negative peaks.

Table 1 shows the different setups of the freely oscillating cantilevered beam carried out for a physical time $Time = 1.50$ s. All cases are configured with the same SPH resolution ($dp = S/4$). However, the number of segments (N) is modified in order to validate the structural behaviour of the FEA solver. It should be noticed that only structure particles are created in this benchmark, so the relevant computational cost to be studied is the consumed one by the multiphysics library. The data reported in the table show that DualSPHysics takes the same computational time as the number of steps remain the same, whereas the number of segments to be solved prevalently affects the Chrono runtime.

5.2. A hydrostatic water column on an elastic beam

A first validation in which FSI phenomenon is relevant is carried out in this section although the physics of this test does not comprise violent collisions and sudden variation of motion. This means that the solution to the problem may be retrieved by uncoupling fluid and structure response still getting high accuracy. In fact, this test case was originally proposed by Fourey [61], as a theoretical configuration to settle a solution of practical interest to compare with. Anyway, it serves well the scope of this section, providing a fair benchmark to evaluating the precision of the numerical solver.

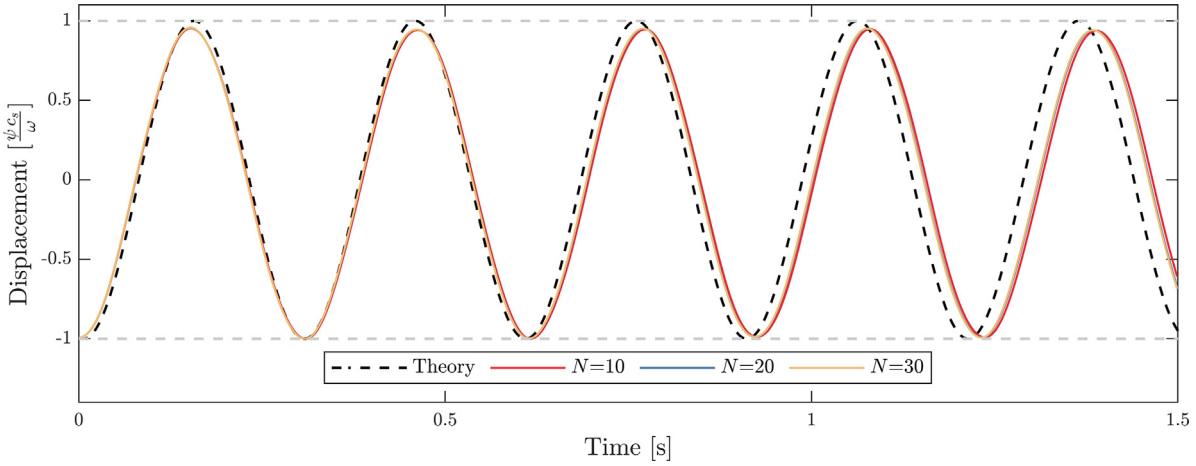

Fig. 9. Time histories of the dimensionless tip deflection (given as a function of the maximum theoretical displacement) of the plate for different number of segments.

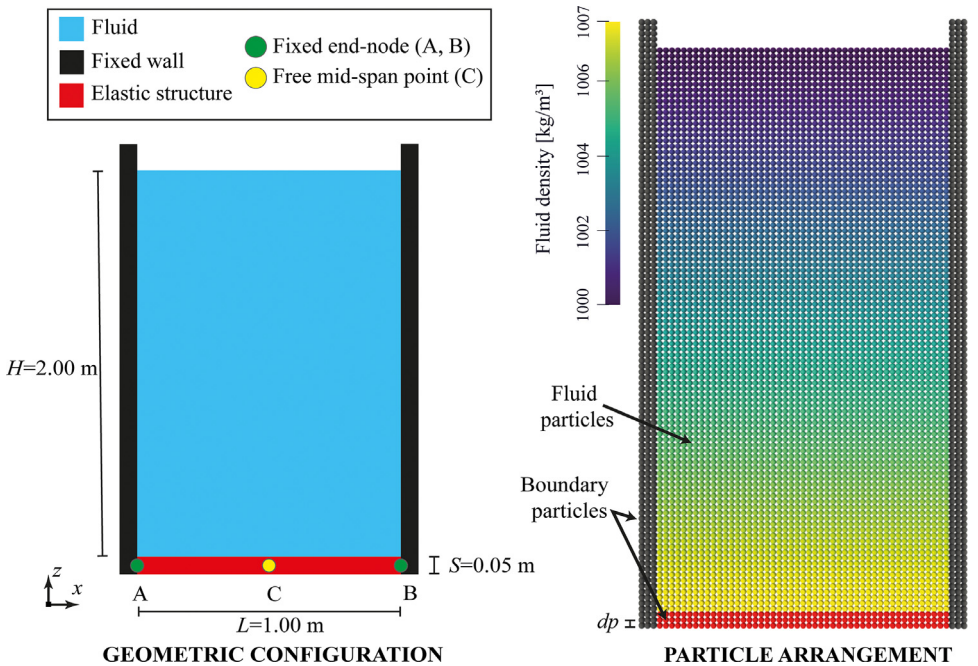

Fig. 10. Initial configuration the hydrostatic water column over an elastic beam and the initial particle arrangement in which the fluid and boundary particles are indicated for the SPH resolution $dp = S/2.5$.

Fig. 10 proposes a schematic sketch of the setup geometry. By assuming that the hydrostatic water column, whose height is $H = 2.00$ m, is at equilibrium on a double-clamped aluminium plate (beam), it allows calculating a closed-form solution of the problem in its initial configuration (straight line). In addition, density $\rho = 1000$ kg/m^3, speed of sound $c_s = 50$ m/s and gravity acceleration as -9.81 m/s^2 are considered. The water column is propped by a 5-centimetre thick ($S = 0.05$ m) and 100-centimetre long ($L = 1.00$ m) aluminium plate, defined with Young's modulus $E = 67.5$ GPa, Poisson's ratio $\nu = 0.34$, and density $\rho = 2700$ kg/m^3. Thus, the deflection of the beam at its mid-span point C, considering that the beam is clamped on both sides (points A and B), is given by:

$$w\,(L/2) = \frac{1}{384} g \frac{(\rho H + \rho_a T)\, L^4}{E_a I_a} \tag{41}$$

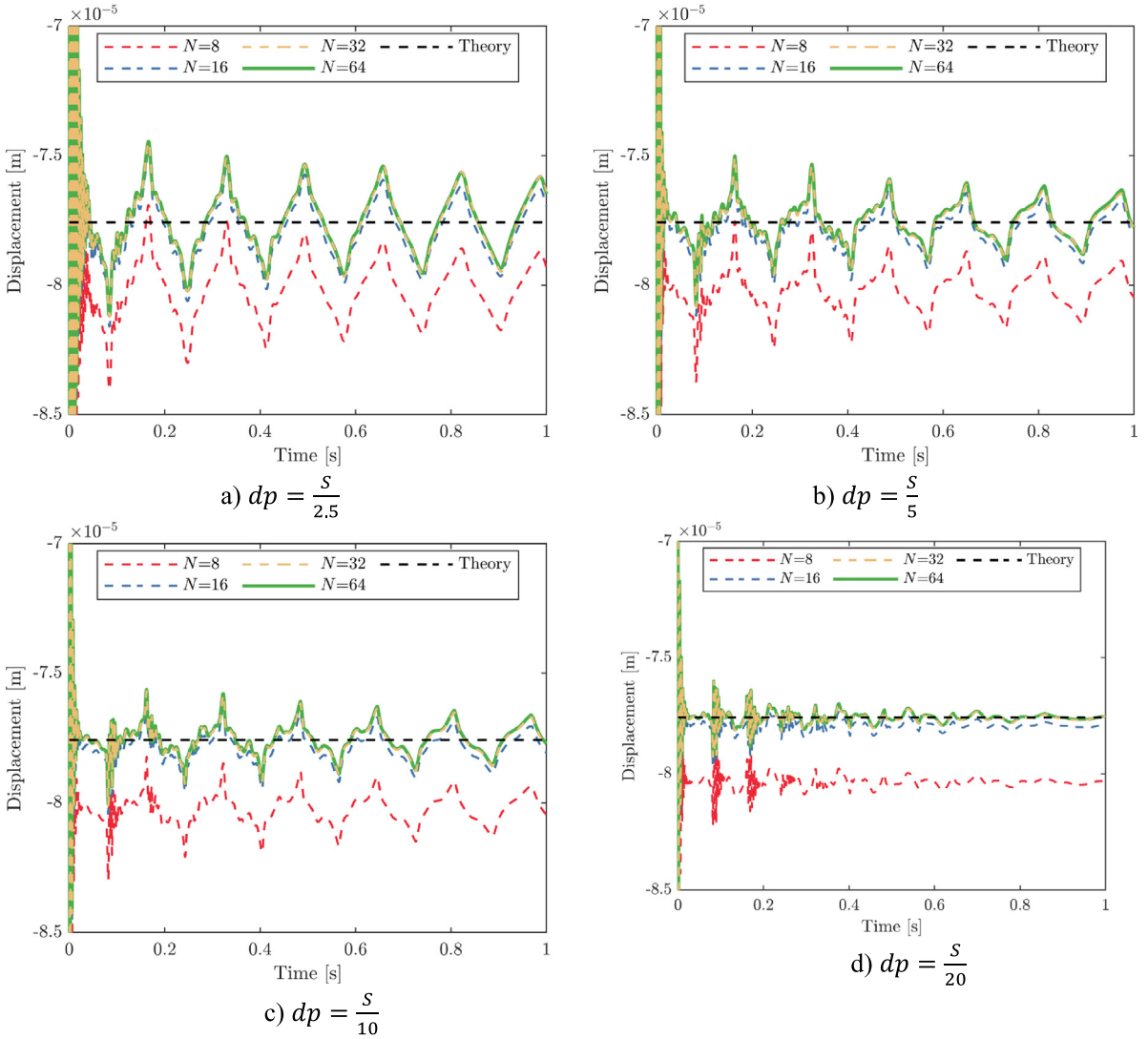

Fig. 11. Displacement history for the mid-span point C for different particle resolutions and number of segments compared to the theoretical solution.

where I_a is the moment of inertia of the beam area. For the problem at hand, Eq. (41) gives a vertical deflection of -77.5 μm, which is itself small, so it resolves to little or no overall movement in the water column. The magnitude of the theoretical displacement, which is several orders of magnitude smaller than the length of the beam, reinforces the quality of the hypotheses on which the utilised beam model grounds, providing a very accurate reference to compare with. It is important to note that for this case there is no need to apply the correction proposed in Eq. (40) because the reference solution is developed with respect to the beam theory rather than the plate theory.

The magnitude of the beam's deflection at its mid-span point (C) justifies the use of this benchmark for defining the accuracy and precision of most FSI coupling procedures. Focusing more on the stability of the technique being used [9,14,17], its use is essentially due to the availability of a highly reliable analytical solution. On this account, it should be emphasised that the use of the double precision for data transfer was critical to correctly capture the plate displacement, being the displacement of the beam many orders of magnitude smaller than the size of the domain.

The dataset is structured in Fig. 11 and corresponds to the outcome of the SPH-FEA coupled model for four different FEM resolutions (number of segments $N = 8$, 16, 32, and 64). Each chart refers to a different initial particle size, respectively, $dp = S/2.5$ (a), $dp = S/5$ (b), $dp = S/10$ (c), and $dp = S/20$ (d), reporting the displacement of

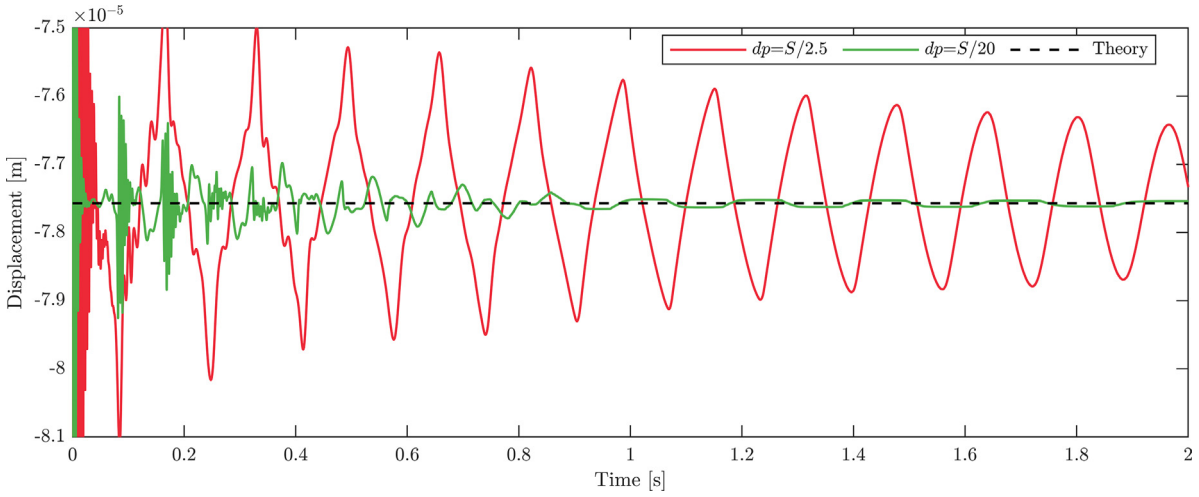

Fig. 12. Particle resolution convergence study for the displacement history at the mid-span point C for 64 FEM segments compared to the theoretical solution.

the control point C against the analytical solution given by Eq. (41), and all the simulations comprise a one-second duration. In this case, when the system response depends on data exchanged between the two solvers, the number of segments mildly affects the accuracy of the whole setup even when boosting the system resolution. This could possibly be due to the low mobility of the fluid particles, which resolves in relatively high accuracy in the fluid force computation regardless of dp. Although the case with $N = 8$ provides low precision, showing a consistent offset from the reference solution of about 3 μm, it exhibits the same overall features of the cases with higher number of segments. Lastly, $N = 16$, $N = 32$, and $N = 64$ provide greater precision, with the latter two fully capturing the analytical solution, as can be clearly seen in panel (d).

Fig. 12 provides an overview on the convergence issue posed by the initial particle resolution dp, while keeping the same number of segments ($N = 64$) for the double-clamped beam. Two main peculiarities of the problem can be clearly appreciated when the problem is solved using the proposed coupling: the particle resolution is game changing in the accuracy and stability of the water column as smaller particle sizes are indicative of less noisy pressure fields. Despite the particle resolution, the fluid forces are well computed in all the cases and thus leading to the same vertical force distributions that eventually provoke the same mid-span deflections.

A better understanding, indeed, on the damped oscillatory nature of the beam mid-point displacement can be grasped by considering the four snapshots in Fig. 13: each one pictures the state of the fluid tank and the beam, with $dp = S/2.5$, at different time steps taken during $Time = 0.001$ s (a), $Time = 0.021$ s (b), $Time = 0.041$ s (c), and $Time = 0.061$ s (d). The time-window covers a range of 0.080 s that corresponds to the return period of occurrence of the spikes that appear in Fig. 11. The cyclic behaviour, marked by large oscillations and clearly visible for coarser particle spacings, is induced by a shock wave, which is likely generated by the initial set down experienced by the beam, propagating vertically in the tank. If one considers that the disturbance is generated at time zero (panel (a) in Fig. 13), the periodicity of the spikes matches perfectly with the travelled distance, which is twice the water column height ($2H$) over the fluid speed of sound c_s. The particle resolution affects the system response since finer particle resolutions allow damping out the pressure disturbance much quickly, resulting in shorter times necessary to stabilise the beam vibrations induced by the pressure wave.

Lastly, Fig. 14 shows a comparison between the pressure measured right above the mid-span point C in the fluid tank for the two resolutions (and $N = 64$) considered above with the analytical pressure computed for still water and no plate deformation. The pressure time histories are affected by the shock wave that forms at time zero, when the water column settles on to the elastic beam. As the particle resolution decreases, the pressure fluctuations seem to reduce as well, and the damping effect provided by the fluid formulation is able to filter out the energy contented of this acoustic wave.

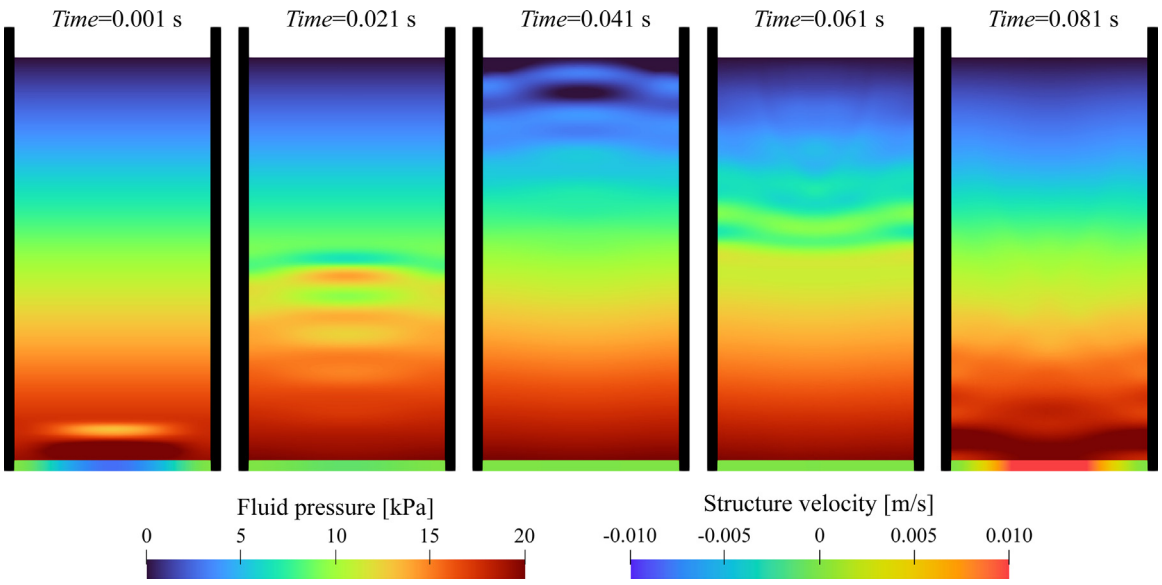

Fig. 13. Snapshots of a one-period pressure wave propagation within the fluid tank with $dp = S/20$, where fluid particles are coloured by pressure whereas solid particles by vertical velocity.

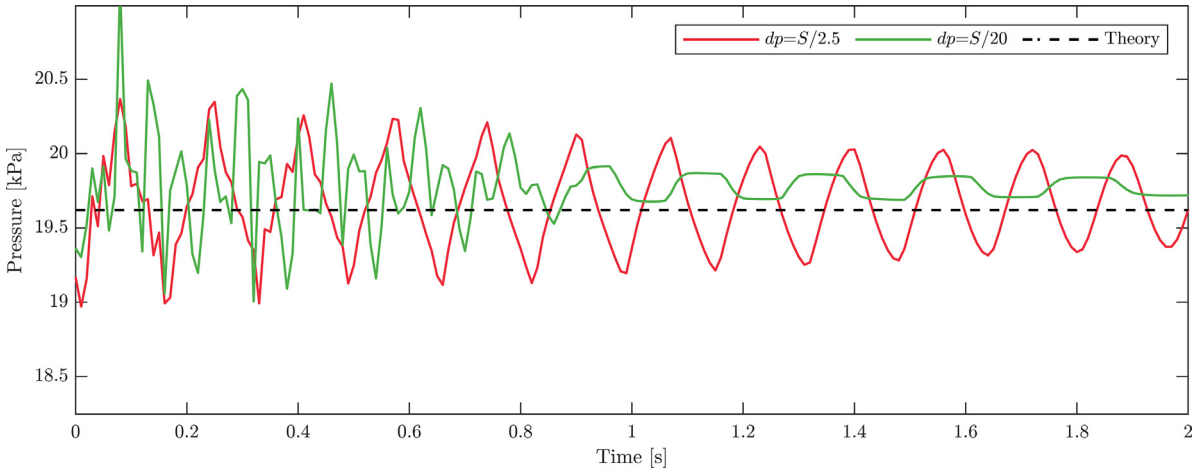

Fig. 14. Fluid pressure time evolution for the mid-span point C for different particle resolutions and $N = 64$ compared to the theoretical solution.

Fig. 15 shows two snapshots corresponding to the fluid pressure and beam stress at the initial state (*Time* = 0 s) and after a while when the system is at the equilibrium (*Time* = 1.00 s), for which pressure field matches the initial state. The initial stage of the water settling on the aluminium beam consists of the water column in its configuration dictated by the presence of gravity alone, whereas the beam is initialised as if gravity were not applied yet. As shown before, the exchange of data process commences soon after the first SPH time step, after which the fluid–structure system starts interacting. The right-hand visual representation proposes the fluid pressure and the beam stress fields for a state at which static conditions have been reached. The stress along the beam (σ_{xx}) shows to be distributed in perfect accordance with the theoretical response of a double clamped beam under a uniform load condition. At the two clamped section, where the beam Boundary Conditions are enforced, the upper fibres are engaged in tension (negative values), whereas the mid cross section proposes a reverse fibre configuration by having the lower ones in tension. Note that the position of the inflection points, in which stress are close to zero (green areas), is perfectly captured as they locate at $0.211L$ from the closest fixed cross section. It is worth mentioning

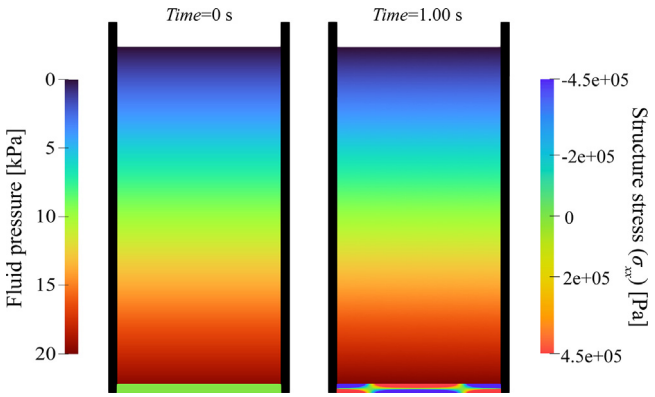

Fig. 15. Snapshots of the simulation considering the fluid pressure and beam stress of the initial state (left) and when the system is at equilibrium (right).

that although the initial shock wave is still travelling, the induced under/over pressure does not cause detectable stress variations in the beam, essentially due to the low magnitude of those pressure oscillations (see Fig. 14).

The accuracy of the coupling is tested with respect to the energy conservation of the structural solver provided by the non-linear FEA solver. As a matter of fact, this case provides proper background for this type of validation considering the total elastic strain energy stored by Euler–Bernoulli beam. With reference to Fig. 3 regarding the nomenclature, the internal energy (U_I) can be defined as:

$$U_I = \frac{1}{2}\int_0^L EI\left(\frac{d^2w}{dx^2}\right)^2 dx \tag{42}$$

Eq. (42) provides, in time, the energy stored by the beam element, and it can be compared with the work done by the external forces. Hence, by considering the work of the external entities acting on a double clamped beam, it can be calculated in a closed form by considering the static displacement function:

$$w\,(x) = -x\frac{q(1-x)(L^2x^2 - L^3x)}{24EIL^2} \tag{43}$$

being $q = (\rho H + \rho_a T)$. By integrating Eq. (42) over the length of the beam, the work of the distributed load is:

$$U_E = \frac{L^5 q}{1440EI} \tag{44}$$

Fig. 16 shows the time evolution of the beam internal energy for an increasing number of beam segments while keeping fixed the SPH particle size to $dp = S/20$, and the numerical model response is compared with the theoretical solution (0.433 J) proposed in Eq. (44). Here, due to the scope of this last test, the simulations are executed for 10.0 s. The chart, proposed in a logarithmic time scale, allows following in detail the initial load process. As mentioned before, the process starts with the beam in a neutral position. At the time the first-time step is computed, the fluid experiences the gravity pull and, therefore the fluid mass finds the beam reactive forces during its fall. Due to the impulsive force that is transferred to the beam, the first instants of the simulation (for all the cases) see a strong increase in the maximum deformation of the beam that, as it can be noticed from the chart, corresponds to a spike in beam internal energy. The first five visibly decaying cycles (up to $Time = 0.02$ s) can be used to characterise the dynamic response of the beam as they are close to the first period of vibration of the system formed by the beam and the part of water it interacts with. The evident damped cyclic response is provided by an energy dissipation that occurs in the fluid phase. From this time on, and up to $Time = 0.080$ s, the beam reaches its equilibrium configuration that matches the theoretical value. Thus, the pressure wave, previously generated by the settling process (see Fig. 13), reaches again the beam-to-fluid interface, thus provoking very small vibrations throughout the beam. The frequency at which those new vibrations take place is close to the previous one, but not exactly the same as the hydrodynamic stiffness offered by the water interface is reduced due to the very small

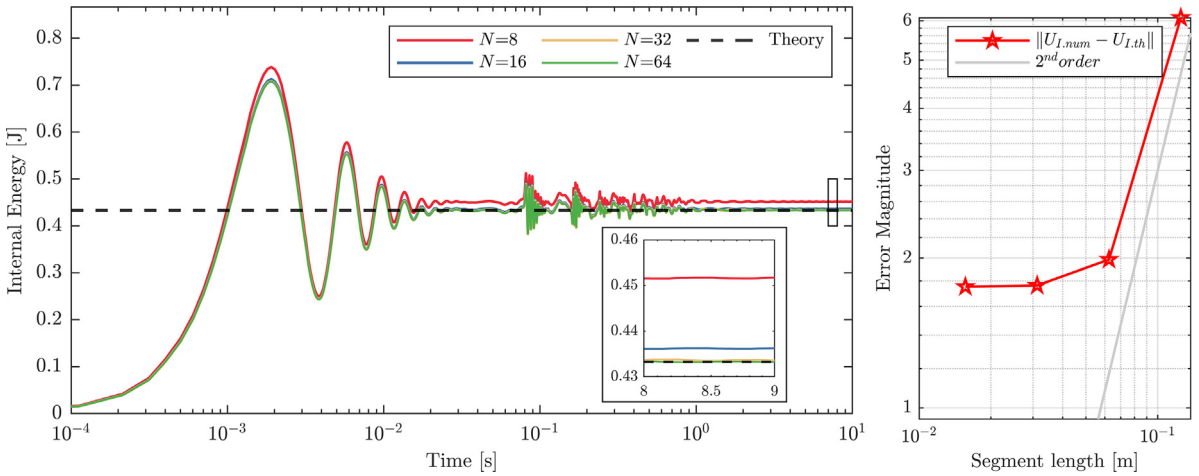

Fig. 16. Total strain energy of the beam compared to the theoretical solution: time history and convergence study.

Table 2
Performance of the hydrostatic water column on an elastic beam case for $N = 64$.

dp	Structure particles	Fluid particles	Segments (N)	SPH steps	DualSPHysics runtime [s]	Chrono runtime [s]	Total runtime [s]	% Chrono
S/2.5	153	6409	64	7383	45	42	87	48
S/5	606	23 106	64	14 775	97	78	175	45
S/10	2211	87 201	64	29 549	192	124	316	39
S/20	8421	338 391	64	59 096	337	183	520	35

overpressure magnitudes. This process iterates for about one second, after which the beam stays steady at its equilibrium position, at which the U_I is consistent with the theoretical value, highlighted by the zoomed view on the time-window from *Time* 8.00 to 9.00 s. For the sake of reference, a similar investigation on the inner energy content of the beam is proposed in [17,62]. The right-hand side of Fig. 16 proposes a converge study by measure of the L_2 error for whole time series, and those values are then reported with respect to the length of segment the beam is discretised with. The chart proposes a close-to-second order convergence rate when moving from the 8 to 16 segments, which is consistent with the time stepper HHT. However, the chart also proves that moving towards finer discretizations does not yield the same rate of convergence. This can be possibly explained by the fact that the resolution of the fluid phase is unchanged, so the overall coupling model hits its saturation state.

The performance results presented in this section include only the combination of each solver's resolution selected with the best of the other solver. Thus, Table 2 shows the performance results of the simulations for different values of *dp* while the number of segments is kept constant ($N = 64$). It can be noticed that the number of particles is varying and, as it increases, the total runtime grows accordingly. Although the resolution of Project Chrono does not change, its runtime is slightly different when the number of particles rises. This trend is possibly due to the increasing number of SPH steps, which is not constant for each simulation because the SPH solver uses a variable integration time step (Δt_{SPH}) that depends on the resolution (h in Eq. (18)). Therefore, when the number of calls to the multiphysics library to solve a time step rises, it causes an additional overhead even though the percentage (%) of time consumed by Chrono is within a narrow range for each case.

On the other hand, Table 3 shows the performance results of the simulations for different values of segments (N), in which the SPH resolution does not change ($dp = S/20$). For all the cases, the number of particles is the same, while the DualSPHysics runtime and the number of SPH steps do not remain constant. More specifically, the runtime of DualSPHysics can indirectly be affected by the number of segments since the SPH solver has to compute the fluid forces for each FEA beam node ($N + 1$) (see Section 4.2). Thus, when the number of segments increases, even if for a constant value of *dp*, the DualSPHysics runtime can be also affected. On the other hand, the number

Table 3
Performance of the hydrostatic water column on an elastic beam case for $dp = S/20$.

dp	Structure particles	Fluid particles	Segments (N)	SPH steps	DualSPHysics runtime [s]	Chrono runtime [s]	Total runtime [s]	% Chrono
$S/20$	8421	338 391	8	59 095	289	45	334	14
$S/20$	8421	338 391	16	59 097	290	52	342	15
$S/20$	8421	338 391	32	59 093	292	77	369	21
$S/20$	8421	338 391	64	59 096	337	183	520	35

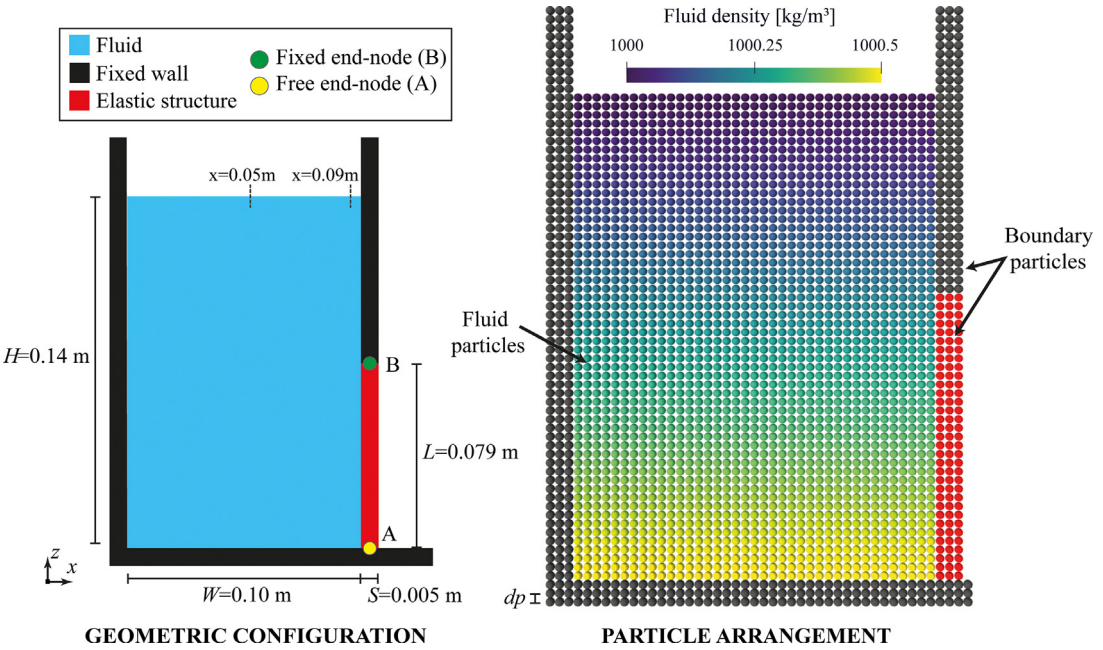

Fig. 17. Initial configuration of the elastic gate, the breaking water column, and its particle discretisation for the SPH resolution $dp = S/2$.

of SPH steps is slightly different since the variable time step used in the SPH solver is computed according to the maximum particle velocity. Therefore, any variation in the response of the FEA model when solving the structure can provoke changes in the Δt_{SPH}. Finally, it can be noticed that the execution time of Project Chrono and the percentage (%) of elapsed time consumption rises according to the number of segments.

5.3. A breaking water-column with an elastic gate

The third case makes use of an experimentally tested setup that was first presented in Antoci et al. [63], in which the experimental set-up and results in a two-dimensional fashion are provided. The schematic of the setup is given in Fig. 17, where a water column, with dimensions height $H = 0.14$ m and width $W = 0.10$ m, is confined between vertical walls. The vertical wall on the right terminates with a 7.90-mm elastic gate (length $L = 0.079$ m, thickness $S = 0.005$ m), clamped to the upper part of a fixed support (node B) and otherwise free to deflect in any direction. Moreover, density $\rho = 1000$ kg/m^3, speed of sound $c_s = 50$ m/s, and gravity acceleration as -9.81 m/s^2 are considered. The elasticity of the gate is modelled using a beam element as proposed by the SPH-FEA scheme to reproduce the deformation induced by the fluid pressure. As final note, it is important to mention that the experimental data (beam free-end and water level in the tank time histories) given in [63] evidently refers to a 3-D case. However, the setup was conceived and ran expecting that the response of the system was not affected by the extension in the third dimension (i.e., width of the tank), so that a bi-dimensional cross section

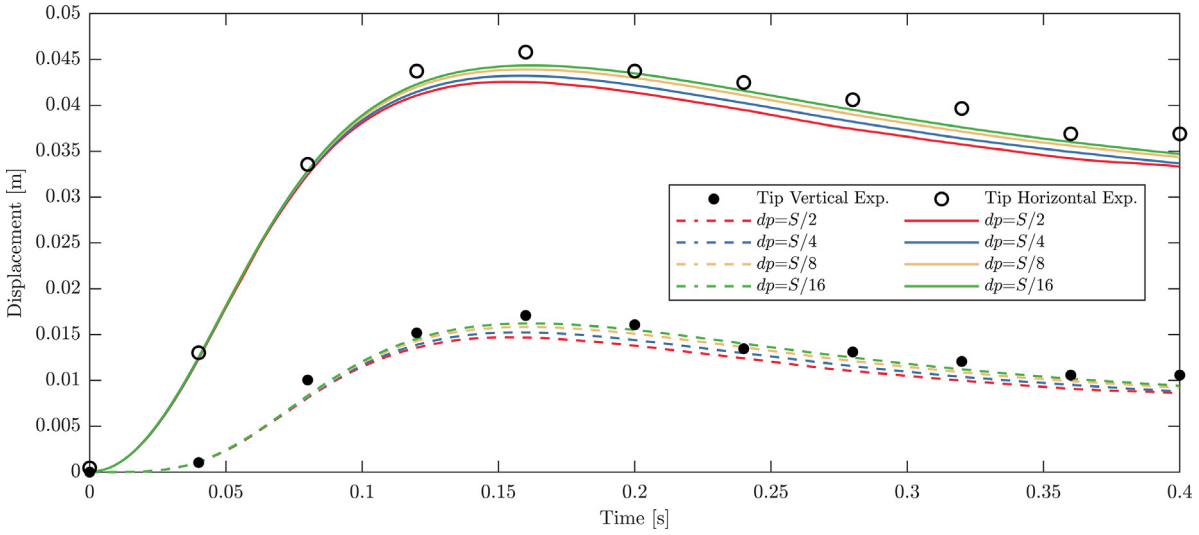

Fig. 18. Horizontal and vertical displacement histories for the tip of the beam (point A) for different particle resolutions and $N = 32$ compared to the experimental reference [63].

Table 4
RMSE estimation between experimental and numerical results for horizontal and vertical displacement of the tip of the beam (point A).

Displacement	Horizontal				Vertical			
dp	*S/2*	*S/4*	*S/8*	*S/16*	*S/2*	*S/4*	*S/8*	*S/16*
RSME	0.0027	0.0022	0.0016	0.0012	0.0017	0.0014	0.0010	0.0008

could well represent the overall system evolution. Fig. 17 reports a vertical cross section of the system along an axis of symmetry for the system, which is used to configure the 2-D numerical environment for this investigation. To support this assumption, apart from the accuracy that the 2-D model in [63] showed, other researchers have made comparison between 2-D and 3-D cases [64,65], de facto recollecting very small deviations between the two solutions.

In this investigation, the parameters that describe the flexible element configuration have been set in accordance with the reference one (i.e., material density $\rho = 1100$ kg/m^3, Poisson's ratio $\nu = 0.50$), except for some details that are given in the following. Firstly, the rubber plate was approximated by [63] as a linear elastic model with Young's modulus $E = 12$ MPa and Poisson's ratio $\nu = 0.40$. However, in the present work, a more compelling modelling procedure was enforced following the mechanical stress–strain characterisation performed by and reported in [66]. This has led structural solvers with advanced capabilities to implement a hyper-elastic material relationship, and thus improving the model accuracy [8,9,64,67]. Nevertheless, the simulations performed using this coupling employ a linear elasticity model and thus, it is only possible to constrain the beam response to obey an initial Young's modulus defined as the secant modulus from the stress–strain relationship at a strain of 0.02 (available in Fourey et al. [9]), giving back a value of $E = 6.50$ MPa. Lastly, the beam has been modelled with $N = 32$ for all the cases.

The accuracy of the numerical model is investigated by analysing the results shown in Figs. 18 and 19, and also considering the results provided in Table 4. In Fig. 18, the beam tip displacement in the vertical (dashed lines) and the horizontal (solid lines) directions is obtained from four different simulations and compared against the experimental reference. The objective of this plot is to provide an evaluation of the accuracy sensitivity to the particle resolution, as for each simulation a decreasing particle size is used. It can be noticed that the results tend to converge to the reference data when increasing the resolution. Therefore, the four resolutions provide a consistent beam response to the fluid kinematics.

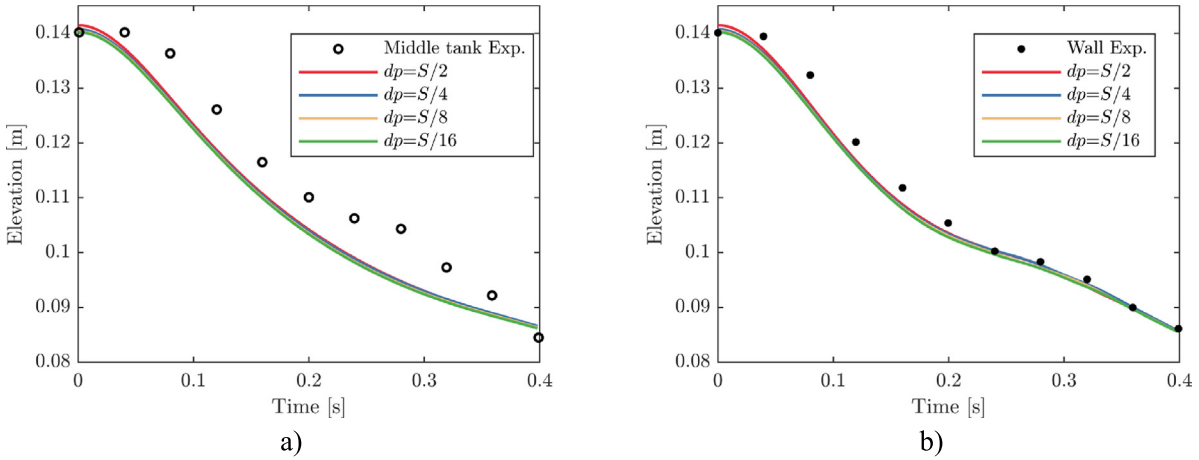

Fig. 19. Water level evolution for different particle resolutions in the middle of the tank (a) and just behind the gate (b).

As anticipated, Table 4 sides the description of this case providing a quantitative assessment of the performance of the model by using the root-mean square error (RMSE) estimator. Thus, the continuous representation provided in Fig. 18 for the numerical model results is first discretised into a set of ten data points that temporally correspond to the experimental sampling time. The RMSE operator processes the dataset and provides the figures that are reported in the following table, for both horizontal and vertical displacement. The results show that the RMSE value decreases with increasing resolution for both horizontal and vertical displacements of the tip. Therefore, studied numerical configurations provide a similar accuracy on account of the experimental solution and provide a clear convergence trend to the reference experimental solution as well.

Fig. 19 shows a comparison of the water level in the middle of the tank (x = 0.05 m) and close to the gate's wall (x = 0.09 m), with only the lowest resolution deviating from the numerical trend established by the others. From the two charts in Fig. 19, it is clear that the numerical model is able to capture the overall water discharge phenomenon, except for a persistent in-time overestimation. On this account, the reference paper [63] reports a similar deviation for the water level evolution at the two locations, explaining that the faster water discharge observed in the numerical model would likely be due to an excess of initial deformation in the beam. Conversely, another investigative work by [9] that provides a similar comparison, suggested that there might be a time shift between the reference displacement and the water level data. The authors lean for the latter reasoning since a slight time shift in the water discharge would deliver much closer agreement and, at the same time, since it is more plausible on account of the accuracy shown by the model in retracing the gate motion.

In closing, six rendered views of the simulations are proposed in Fig. 20 for six-time steps where the two separated colour bars indicate the fluid pressure and structure stress, respectively. They correspond to the beginning of the water discharge (first row), where the beam experiences sudden changes in the beam stress distribution, then the level of stress becomes gradually steadier as the water discharge increases. From the fourth (second row) it can be noticed that the beam achieves a sort of stationary posture, where the fluid forces are at equilibrium with the elastic recentring force of the system (Fig. 18 from *Time* = 0.16 s). Note that the beam stress field here is almost unchanged from one snapshot to the other, and this reflects the small variation in maximum displacement.

Furthermore, Fig. 21 shows the instant of the simulation when the tip of the elastic structure reaches its maximum deflection (*Time* = 0.16 s), where the fluid pressure and the stress field for the elastic gate are represented considering the SPH resolution *dp* = S/16. This much more zoomed visualisation of the numerical configuration captured at a given time offers the possibility to appreciate the quality of the resolved pressure field, which is very smooth. Such smoothness is preserved at the discharge cross section that develops soon after the tip of the beam, where a new free surface and the pressure gradient is the highest. On the other hand, the zoomed representation of the beam confirms equally high quality in the stress response. The spectrum of the colour bar that indicates beam stress in such that blue refers to the tension and red, compression. Two main features may be immediately apparent from the figures, and they are a direct consequence of the employed model to describe the beam. First, the range is perfectly

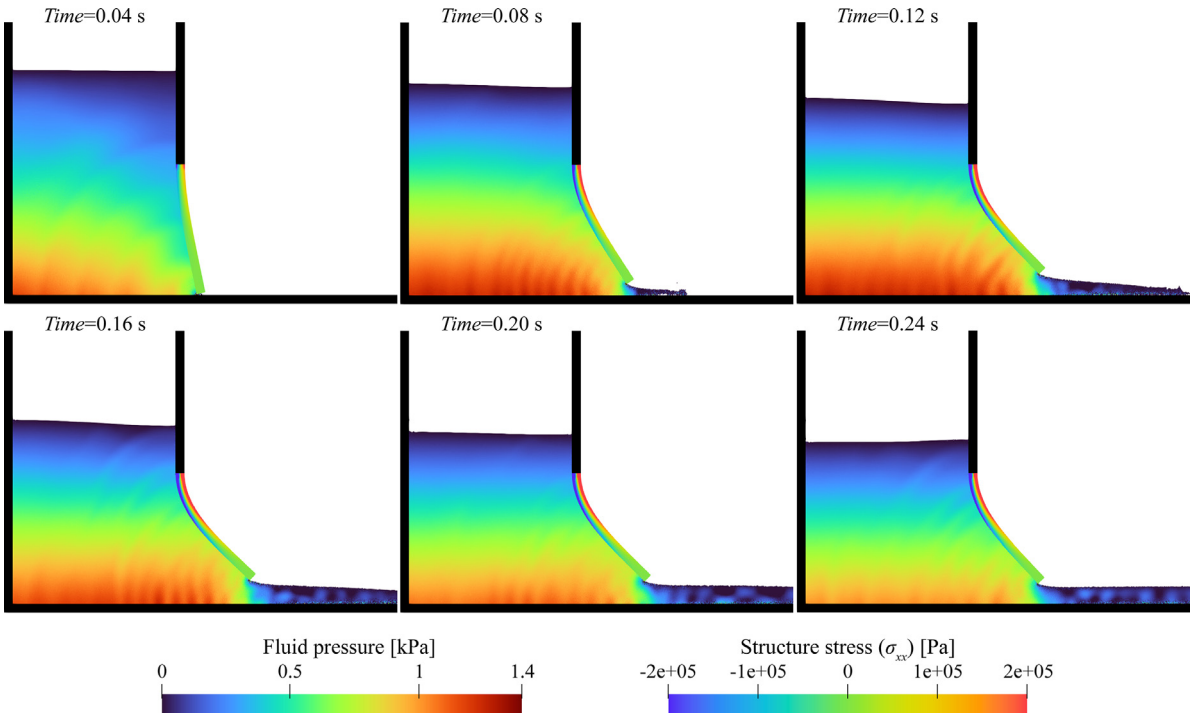

Fig. 20. Snapshots of the simulation of the elastic gate with $dp = S/16$ in which the fluid pressure and structure stress are represented.

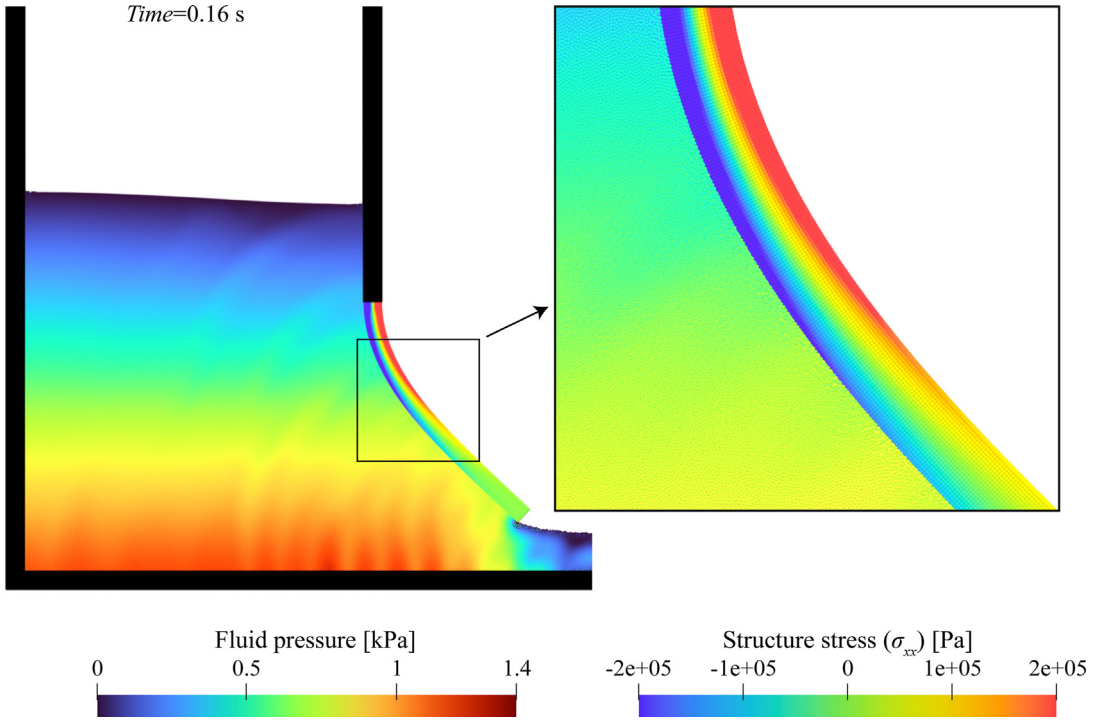

Fig. 21. Fluid pressure and structure stress at $Time = 0.16$ s of the elastic gate case where the structure experiences the maximum deflection.

Table 5
Performance of the breaking water-column with an elastic gate case for $N = 32$.

dp	Structure particles	Fluid particles	Segments (N)	SPH steps	DualSPHysics runtime [s]	Chrono runtime [s]	Total runtime [s]	% Chrono
S/2	99	2184	32	30 724	108	126	235	54
S/4	320	8848	32	61 547	300	251	551	45
S/8	1143	35 612	32	122 761	641	466	1106	42
S/16	4318	142 912	32	244 922	1609	995	2604	38

symmetric, and it results from the fact that fluid actions are (axial and longitudinal ones) computed using the SPH boundary particles, but then they are applied to the nodes located on the axis of the beam. Secondly, there is a layer of particles, located in the middle of the beam (neutral axis) that does not experience any stress due to the fact that only the bending moment is considered, thus not having axial forces. Note that the selected range for σ_{xx} allows describing fully the stress value spectrum and thus comparison can be visually made to other references such as (Zhang et al. [68]).

Table 5 shows the performance results for the third benchmark presented in this work, defining four different SPH resolutions ($dp = S/2$, $dp = S/4$, $dp = S/8$ and $dp = S/16$). In all the cases, the beam is modelled with $N = 32$, and a physical time $Time = 0.40$ s is simulated. When the number of particles simulated increases, due to the use of progressively finer interparticle spacings, both the DualSPHysics runtime and the SPH time steps proportionally increase. Likewise, as it can be noticed from the seventh column, the Project Chrono runtime is influenced in spite of having a constant resolution of the FEA solver. This occurs due to the growing number of calls to the FEA solver that corresponds to the SPH steps. This fact is clear when the percentage of time consumed by Project Chrono is considered, which is quite similar in all cases.

5.4. A dam break impacting a flexible obstacle

In contrast with the testing performed prior within this paper, the nature of the fourth benchmark comprises a much violent fluid–structure interaction, characterised by large displacements and harsh accelerations of the solid phase with respect to the fluid one. The test proposed by Liao et al. [69] comprises a breaking water column impacting a rubber plate in a 3-D confined environment, in which multi-phase effects become relevant for the correct simulation of the obstacle displacement. Within the scope of this research, the impact of the water column and the flow over the flexible obstacle is taken as a reference up to 0.80 s because the multiphase water–air interaction that happens after cannot be captured by the present solver. The sketch of the problem is given in Fig. 22. In the experiment, the elastic baffle is made of rubber with thickness $S = 0.004$ m, length $L = 0.090$ m, density $\rho = 1161.54$ kg/m^3, and Young's modulus $E = 3.50$ MPa. The plate is placed vertically at 0.40 m away from the right-hand side of the water column, and it is deployed such a way that the cross section indicated by point A can be considered the only boundary surface clamped to the experimental water tank. On the other hand, point B is considered representative of the free end of this cantilevered plate. It is important to mention at this stage that the plate width takes up the whole width of the tank (0.10 m), and as so happens, this is very handy as the dynamics of the system is well represented by its middle plane, providing the basis for testing numerical solvers considering 2-D environments. During the test, the motion of the baffle was monitored using a visual tracking system, and the motion for three markers was recorded; in the following, data that refers to Marker 1 (0.0875 m above the tank bottom) is used for comparison purposes.

For the numerical model, the water column height $H = 0.20$ m is discretised with density $\rho = 997$ kg/m^3 and using a speed of sound $c_s = 50$ m/s. It is kept still up to time zero, when the removable gate starts moving upward at an imposed velocity that corresponds to the motion law given in the reference work. The flexible plate comprises $N = 32$ Euler–Bernoulli beam segments with the following properties: a corrected Young's modulus $\hat{E} = 4.39$ MPa is obtained from Eq. (40) and Poisson's ratio $\nu = 0.45$. The numerical discretisation for a resolution that corresponds to $dp =$ S/4 (1 mm) is visualised in Fig. 22.

Four SPH resolutions are considered ($dp = S/4$, $dp = S/8$, $dp = S/16$ and $dp = S/32$), while keeping a fixed number of segments ($N = 32$) to solve this benchmark numerically. The response of the solver for the four cases listed before is arranged in a chart and reported in Fig. 23 by comparing the experimental data for the horizontal

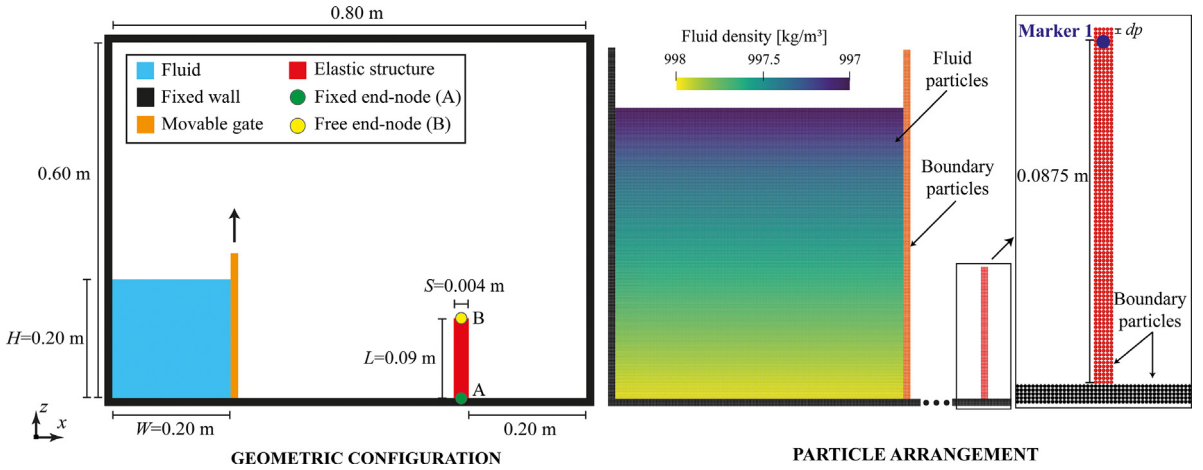

Fig. 22. Initial configuration of the dam break impacting a flexible obstacle and its particle discretisation for the SPH resolution $dp = S/4$.

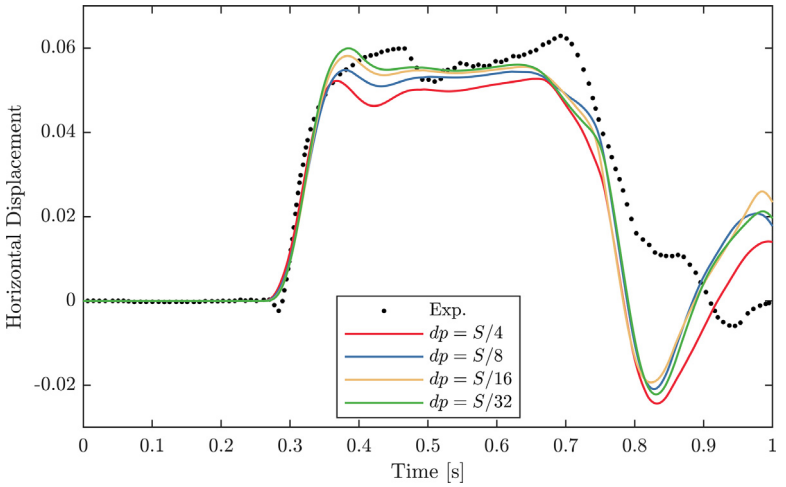

Fig. 23. Horizontal displacement histories for the tip of the beam (Marker 1) for different particle resolutions (dp) and $N = 32$ compared to the experimental reference [69].

displacement of Marker 1 [69] against the same quantity computed from the numerical simulations. The description of this test case is further completed by Fig. 24 that shows six visualisations at relevant steps, which collect particle information on the fluid pressure (colour bar on the left) and structure stress (colour bar on the right).

The model predicts the response of the beam under the free-surface flow impact up to $Time = 0.50$ s, whereas it drops in agreement due to the influence of the air phase on the overall dynamic of the fluid phase, as suggested by previous literature dealing with this case. A more detailed discussion can be found in Liao et al. [69] and in Sun et al. [11] on the effect of multi-phase interaction on the accuracy of this specific problem. Regardless, this benchmark is very useful to test the stability and accuracy of FSI solvers. The proposed one shows similar features to other single-phase solvers (see for instance Khayyer et al. [70] and O'Connor & Rogers [14]). More specifically, the impact instant, which mostly depends on the accuracy of the fluid phase is well captured by providing a consistent and precise instant for the four resolutions around $Time = 0.27$ s (first frame of Fig. 24). From this point on, the impact of the waterfront resolves in sudden beam deformations, which start cumulating as the tip of the beam goes towards its maximum deformation. Around $Time = 0.32$ s (second frame of Fig. 24), the fluid mass is deflected by the beam, which in turn, experiences a deformed shape comprising two changes in curvature. However, the accuracy during this phase indicates quite remarkable sensitivity to the fluid resolution, as the displacement of the beam tends

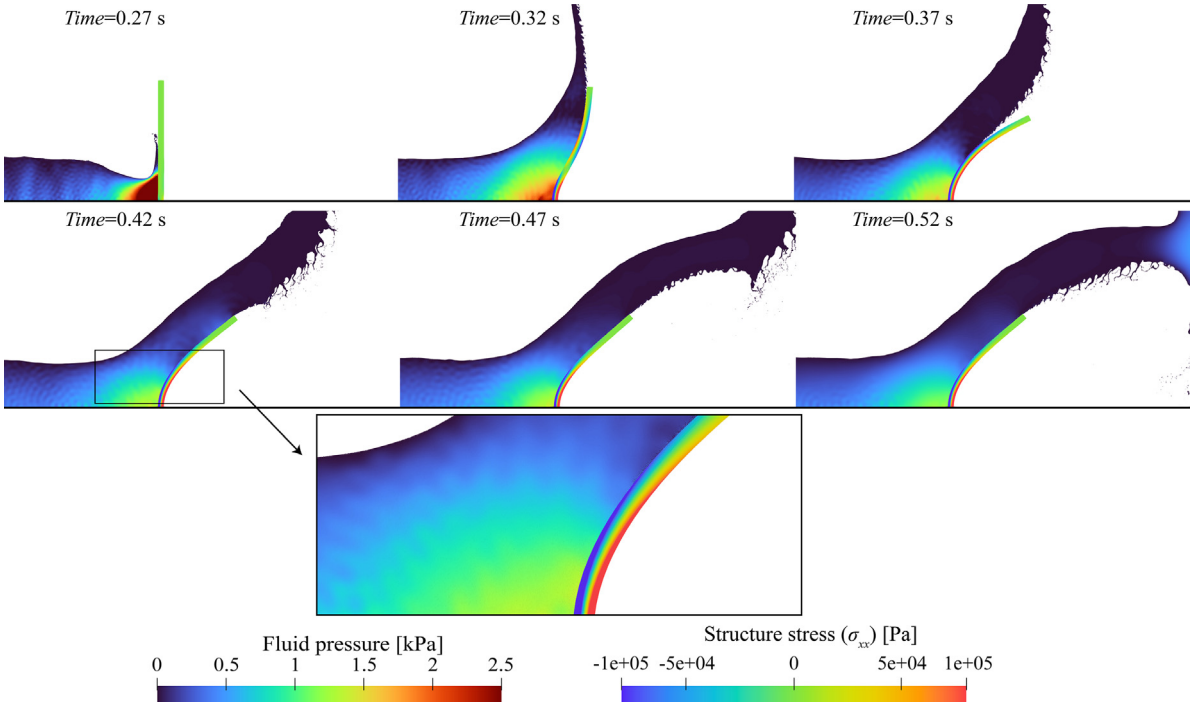

Fig. 24. Snapshots of the simulation of dam break impacting a flexible obstacle with $dp = S/32$ in which the fluid pressure and structure stress are represented.

towards a maximum displacement of around 0.06 m, and this is highlighted in the third frame of Fig. 24. The beam, at this instant, has shifted its deformed shape to show a linear bending moment distribution. Note that the tip of the beam has slightly detached the fluid main flow due to a *backlash* effect. The ensuing phase is characterised by a sort of steady state due to a substantial constant flow that maintains an almost constant state of stress in the beam, as shown in the fourth and fifth frames in Fig. 24. Lastly, the sixth frame in Fig. 24 determines the point at which the multiphase air–water interaction begins due to the trapped air below the flow that is still in contact with the lateral wall. However, this does not become apparent in terms of beam deflection till $Time = 0.60$ s when the horizontal displacement diverges from the reference solution. After this, the response of the system is no longer consistent since the air trapped in the cavity that forms downstream of the beam heavily affects the hydrodynamics of the system [11]. It is also included a zoomed view of the snapshot that corresponds to $Time = 0.42$ s, where it can be seen the representation of the stress along the beam.

Table 6 shows the performance results for the fourth benchmark presented in this work, where a physical time $Time = 1.00$ s is simulated. The four different SPH resolutions ($dp = S/4$, $dp = S/8$, $dp = S/16$ and $dp = S/32$) are performed, while the beam is modelled with $N = 32$ for all the cases. It can be noticed that when the number of particles simulated increases, due to the use of higher SPH resolutions, both the DualSPHysics runtime and the SPH time steps increase accordingly. Moreover, the Project Chrono runtime is slightly affected by the SPH resolution, due to the growing number of calls to the FEA solver that corresponds to the SPH steps. However, the percentage of time consumed by Project Chrono decreases when the number of particles increase. Regarding the highest SPH resolution reported here ($dp = S/32$), which corresponds to more than 2.5 million of fluid particles, the computational cost of solving the structure is 15% of the total runtime.

6. Conclusions and future work

This paper has presented a novel SPH-FEA solver coupling between the open source DualSPHysics and the Project Chrono library. The outcome software leverages the meshless SPH method to deal with the resolution of

Table 6
Performance of the flexible obstacle case for $N = 32$.

dp	Structure particles	Fluid particles	Segments (N)	SPH steps	DualSPHysics runtime [s]	Chrono runtime [s]	Total runtime [s]	% Chrono
S/4	455	40 401	32	158 938	1299	619	1918	32
S/8	1629	160 801	32	322 158	3864	1120	4984	22
S/16	6137	641 601	32	676 281	8824	2252	11 076	20
S/32	23 793	2 563 200	32	1 342 800	35 990	6406	42 396	15

the Navier–Stokes' equations to simulate fluid phases, whereas the non-linear FEM-based FEA module herein solves the dynamics of elastic structures. The proposed coupled method offers many advantages for the simulations of FSI problems thanks to the blending of the two solvers. On the one hand, the strength of the SPH-based fluid solver, very powerful in addressing violent flows and dealing with free-surface flows. On the other, the relatively inexpensive Euler–Bernoulli beam model and the Lagrangian capabilities of the Corotational framework for flexible elements capable of accommodating large displacements. Ultimately, it is important to mention that the structure of the two-way algorithm herein presented, in which the two systems communicate via exchanging forces and positions, has demonstrated to be extremely robust and thus providing a key distinctive feature to this new implementation: *uncoupled resolutions*.

Following an increasing level of complexity, four standardised validation cases have been proposed as references to validate the numerical framework. Firstly, the numerical prediction for a freely oscillating cantilevered beam, in which the motion is induced by very specific initial conditions, was validated contrasting with an analytical solution. The comparison shows a satisfactory matching, though overestimating the fundamental (or first) period of vibration of the structural system within a 2-% range, whereas perfectly capturing the motion amplitude. This initial investigation was critical for assessing minimum requirements to optimise the beam mesh, and the accuracy that the structural solver requires to perform the subsequent validation tasks.

Secondly, a proper case of fluid interacting with a structure has been set up. Despite its simplicity, a double-clamped horizontal beam supporting a pseudo-static water column has revealed to be extremely useful in estimating the model precision, as widely recognised in the reported literature. Again, a theoretical solution, based on legitimated hypotheses, provides the reference framework to compare with, and the proposed model shows accuracy in estimating the beam mid-point displacement. Additionally, the energy dissipation of the structural integrator has been thoroughly checked for long simulations. The results provided another metric to highlight the accuracy and precision of the solver, but in more general terms, they allow us to remark the coupling strategy ensures the energy conservation of the system. The results sourced from the performed simulations highlight the pros of having the uncoupled-resolution feature, which, in principle, allows to tune the model in accordance with the expected response of the system, thus smartly allocating the computational resources.

Thirdly, the discharge of a water reservoir adjusted by a flexible gate has been simulated following the experimental setup investigated in [63]. The surface of the elastic element (the gate) interacts with a medium-speed flow that also develops relevant interactions between the beam's displacement and the fluid transient states. Relatively low fluid resolutions delivered good agreement on account of a well-resolved beam kinematics, and, as the results showed, the first investigated case fails in estimating the beam deflection only when the particle size hampers the correct prediction of the water discharge, essentially correlated to the fluid resolution.

Lastly, the fourth case achieves the maximum level of complexity among the cases presented in this paper. A breaking water column runs over a flexible beam which in an initial phase deflects the flow that then chaotically scatters across the whole closed environment. Again, the numerical model successfully predicts the overall FSI system dynamics, while proving very resilient to such extreme spatial changes. The sensitivity analysis that was performed by considering both solid and fluid phases proved that even cases with a very limited number of particle layers can suffice. It should be noted that the air phase was not simulated in this work. Therefore, the reported numerical results are not in perfect agreement when the influence of the air phase on the overall dynamic of the fluid phase plays an important role, as discussed in [11].

In this work, the proposed coupling has been described and used with respect to a two-dimensional environment, but its extension to a 3-D one should be theoretically possible. Future work will comprise the implementation and validations of the presented framework for 3-D simulations, for which the effect of rotational forces or torques on the

nodes will be considered for experiencing bending and torsion in the beam. To sum up, the extension will keep using Euler–Bernoulli-based beam elements that, in spite of being capable of describing only particular physical systems, can provide an excellent balance between the solid solver computational cost and the quality of the outcome. It is expected that the impact of computational performance of the structural solver will greatly diminish when moving to full 3-D simulations, as its cost will mostly stay the same while the fluid simulation runtime will be dominant.

In addition, future implementation will contain a builder for structural systems that can comprise multiple beams assembled together to form any structure configuration, on which the use of the Rayleigh damping model will be activated. As it is the writing of this paper, multiphysics simulations comprising free surface flows and flexible elements in 3D are still restricted to academic cases and have not yet seen applications to engineering problems mainly due to their prohibitive computational cost.

Declaration of competing interest

The authors declare that they have no known competing financial interests or personal relationships that could have appeared to influence the work reported in this paper.

Data availability

Data will be made available on request.

Acknowledgements

Funding for open access charge: Universidade de Vigo/CISUG, Spain. This work was supported by the project SURVIWEC PID2020-113245RB-I00 financed by Ministerio de Ciencia e Innovación (MCIN/AEI/10.13039/501100011033) and by the project ED431C 2021/44 *"Programa de Consolidación e Estructuración de Unidades de Investigación Competitivas" financed by Xunta de Galicia*, *Consellería de Cultura, Educación e Universidade*. This study forms part of the Marine Science programme (ThinkInAzul) supported by *Ministerio de Ciencia e Innovación and Xunta de Galicia* with funding from European Union NextGenerationEU (PRTR-C17.I1) and European Maritime and Fisheries Fund. Grant TED2021-129479A-I00 funded by Ministerio de Ciencia e Innovación (MCIN/AEI/10.13039/501100011033) and by the "European Union NextGenerationEU/PRTR".

I. Martínez-Estévez acknowledges funding from *Xunta de Galicia* under *"Programa de axudas á etapa predoutoral da Consellería de Cultura, Educación e Universidades da Xunta de Galicia"* (ED481A-2021/337). J. El Rahi is a Ph.D. fellow (fellowship 1115821N) of the Research Foundation Flanders (FWO). B. Tagliafierro acknowledges financial support for this publication by the Fulbright Schuman Program, which is administered by the Fulbright Commission in Brussels and jointly financed by the U.S. Department of State, and the Directorate-General for Education, Youth, Sport and Culture (DG.EAC) of the European Commission. Its contents are solely the responsibility of the authors and do not necessarily represent the official views of the Fulbright Program, the Government of the United States, or the Fulbright Commission in Brussels. The authors wish to acknowledge the support provided by the Project Chrono developers: Prof. Dan Negrut and Dr. Radu Serban (University of Wisconsin–Madison, US), and Prof. Alessandro Tasora (University of Parma, Italy).

References

[1] M.S. Shadloo, G. Oger, D. Le Touzé, Smoothed particle hydrodynamics method for fluid flows, towards industrial applications: Motivations, current state, and challenges, Comput. Fluids 136 (2016) 11–34, http://dx.doi.org/10.1016/j.compfluid.2016.05.029.

[2] M.-C. Hsu, Y. Bazilevs, Fluid–structure interaction modeling of wind turbines: simulating the full machine, Comput. Mech. 50 (2012) 821–833, http://dx.doi.org/10.1007/s00466-012-0772-0.

[3] R. Roul, A. Kumar, Fluid-structure interaction of wind turbine blade using four different materials: Numerical investigation, Symmetry 12 (2020) 1467, http://dx.doi.org/10.3390/sym12091467.

[4] F.-B. Tian, H. Dai, H. Luo, J.F. Doyle, B. Rousseau, Fluid–structure interaction involving large deformations: 3D simulations and applications to biological systems, J. Comput. Phys. 258 (2014) 451–469, http://dx.doi.org/10.1016/j.jcp.2013.10.047.

[5] S. Bailoor, A. Annangi, J.H. Seo, R. Bhardwaj, Fluid–structure interaction solver for compressible flows with applications to blast loading on thin elastic structures, Appl. Math. Model. 52 (2017) 470–492, http://dx.doi.org/10.1016/j.apm.2017.05.038.

[6] D.J. Benson, Computational methods in Lagrangian and Eulerian hydrocodes, Comput. Methods Appl. Mech. Eng. 99 (1992) 235–394, http://dx.doi.org/10.1016/0045-7825(92)90042-I.

[7] A. Khayyer, H. Gotoh, Y. Shimizu, On systematic development of FSI solvers in the context of particle methods, J. Hydrodyn. 34 (2022) 395–407, http://dx.doi.org/10.1007/s42241-022-0042-3.
[8] Z. Li, J. Leduc, J. Nunez-Ramirez, A. Combescure, J.-C. Marongiu, A non-intrusive partitioned approach to couple smoothed particle hydrodynamics and finite element methods for transient fluid–structure interaction problems with large interface motion, Comput. Mech. 55 (2015) 697–718, http://dx.doi.org/10.1007/s00466-015-1131-8.
[9] G. Fourey, C. Hermange, D. Le Touzé, G. Oger, An efficient FSI coupling strategy between Smoothed Particle Hydrodynamics and Finite Element methods, Comput. Phys. Commun. 217 (2017) 66–81, http://dx.doi.org/10.1016/j.cpc.2017.04.005.
[10] C. Chen, W.-K. Shi, Y.-M. Shen, J.-Q. Chen, A.-M. Zhang, A multi-resolution SPH-FEM method for fluid–structure interactions, Comput. Methods Appl. Mech. Eng. 401 (2022) 115659, http://dx.doi.org/10.1016/j.cma.2022.115659.
[11] P.N. Sun, D. Le Touzé, A.-M. Zhang, Study of a complex fluid–structure dam-breaking benchmark problem using a multi-phase SPH method with APR, Eng. Anal. Bound. Elem. 104 (2019) 240–258, http://dx.doi.org/10.1016/j.enganabound.2019.03.033.
[12] P.-N. Sun, D. Le Touzé, G. Oger, A.-M. Zhang, An accurate FSI-SPH modeling of challenging fluid–structure interaction problems in two and three dimensions, Ocean Eng. 221 (2021) 108552, http://dx.doi.org/10.1016/j.oceaneng.2020.108552.
[13] S. Capasso, B. Tagliafierro, I. Martínez-Estévez, J.M. Domínguez, A.J.C. Crespo, G. Viccione, A DEM approach for simulating flexible beam elements with the Project Chrono core module in DualSPHysics, Comput. Part. Mech. 9 (2022) 969–985, http://dx.doi.org/10.1007/s40571-021-00451-9.
[14] J. O'Connor, B.D. Rogers, A fluid–structure interaction model for free-surface flows and flexible structures using smoothed particle hydrodynamics on a GPU, J. Fluids Struct. 104 (2021) 103312, http://dx.doi.org/10.1016/j.jfluidstructs.2021.103312.
[15] Y. Ren, A. Khayyer, P. Lin, X. Hu, Numerical modeling of sloshing flow interaction with an elastic baffle using SPHinXsys, Ocean Eng. 267 (2023) 113110, http://dx.doi.org/10.1016/j.oceaneng.2022.113110.
[16] A.M.A. Nasar, B.D. Rogers, A. Revell, P.K. Stansby, Flexible slender body fluid interaction: Vector-based discrete element method with Eulerian smoothed particle hydrodynamics, Comput. Fluids 179 (2019) 563–578, http://dx.doi.org/10.1016/j.compfluid.2018.11.024.
[17] A. Khayyer, H. Gotoh, H. Falahaty, Y. Shimizu, An enhanced ISPH–SPH coupled method for simulation of incompressible fluid–elastic structure interactions, Comput. Phys. Commun. 232 (2018) 139–164, http://dx.doi.org/10.1016/j.cpc.2018.05.012.
[18] D.S. Morikawa, M. Asai, Coupling total Lagrangian SPH–EISPH for fluid–structure interaction with large deformed hyperelastic solid bodies, Comput. Methods Appl. Mech. Eng. 381 (2021) 113832, http://dx.doi.org/10.1016/j.cma.2021.113832.
[19] J.J. Monaghan, Smoothed particle hydrodynamics, Rep. Progr. Phys. 68 (2005) 1703, http://dx.doi.org/10.1088/0034-4885/68/8/R01.
[20] E.-S. Lee, C. Moulinec, R. Xu, D. Violeau, D. Laurence, P. Stansby, Comparisons of weakly compressible and truly incompressible algorithms for the SPH mesh free particle method, J. Comput. Phys. 227 (2008) 8417–8436, http://dx.doi.org/10.1016/j.jcp.2008.06.005.
[21] J.J. Monaghan, R.A. Gingold, Shock simulation by the particle method SPH, J. Comput. Phys. 52 (1983) 374–389, http://dx.doi.org/10.1016/0021-9991(83)90036-0.
[22] M. Antuono, A. Colagrossi, S. Marrone, D. Molteni, Free-surface flows solved by means of SPH schemes with numerical diffusive terms, Comput. Phys. Commun. 181 (2010) 532–549, http://dx.doi.org/10.1016/j.cpc.2009.11.002.
[23] A. Khayyer, Y. Shimizu, T. Gotoh, H. Gotoh, Enhanced resolution of the continuity equation in explicit weakly compressible SPH simulations of incompressible free-surface fluid flows, Appl. Math. Model. 116 (2023) 84–121, http://dx.doi.org/10.1016/j.apm.2022.10.037.
[24] D.D. Meringolo, A. Colagrossi, S. Marrone, F. Aristodemo, On the filtering of acoustic components in weakly-compressible SPH simulations, J. Fluids Struct. 70 (2017) 1–23, http://dx.doi.org/10.1016/j.jfluidstructs.2017.01.005.
[25] S.J. Cummins, M. Rudman, An SPH projection method, J. Comput. Phys. 152 (1999) 584–607, http://dx.doi.org/10.1006/jcph.1999.6246.
[26] A. Skillen, S. Lind, P.K. Stansby, B.D. Rogers, Incompressible smoothed particle hydrodynamics (SPH) with reduced temporal noise and generalised Fickian smoothing applied to body–water slam and efficient wave–body interaction, Comput. Methods Appl. Mech. Eng. 265 (2013) 163–173, http://dx.doi.org/10.1016/j.cma.2013.05.017.
[27] J.M. Domínguez, G. Fourtakas, C. Altomare, R.B. Canelas, A. Tafuni, O. García-Feal, I. Martínez-Estévez, A. Mokos, R. Vacondio, A.J.C. Crespo, B.D. Rogers, P.K. Stansby, M. Gómez-Gesteira, DualSPHysics: from fluid dynamics to multiphysics problems, Comput. Part. Mech. 9 (2022) 867–895, http://dx.doi.org/10.1007/s40571-021-00404-2.
[28] J.M. Domínguez, A.J. Crespo, M. Gómez-Gesteira, Optimization strategies for CPU and GPU implementations of a smoothed particle hydrodynamics method, Comput. Phys. Commun. 184 (2013) 617–627.
[29] A. Tasora, R. Serban, H. Mazhar, A. Pazouki, D. Melanz, J. Fleischmann, M. Taylor, H. Sugiyama, D. Negrut, Chrono: An open source multi-physics dynamics engine, in: T. Kozubek, R. Blaheta, J. Šístek, M. Rozložník, M. Čermák (Eds.), High Performance Computing in Science and Engineering, Springer International Publishing, Cham, 2016, pp. 19–49, http://dx.doi.org/10.1007/978-3-319-40361-8_2.
[30] R.B. Canelas, M. Brito, O.G. Feal, J.M. Domínguez, A.J.C. Crespo, Extending DualSPHysics with a Differential Variational Inequality: modeling fluid-mechanism interaction, Appl. Ocean Res. 76 (2018) 88–97, http://dx.doi.org/10.1016/j.apor.2018.04.015.
[31] I. Martínez-Estévez, J.M. Domínguez, B. Tagliafierro, R.B. Canelas, O. García-Feal, A.J.C. Crespo, M. Gómez-Gesteira, Coupling of an SPH-based solver with a multiphysics library, Comput. Phys. Commun. 283 (2023) 108581, http://dx.doi.org/10.1016/j.cpc.2022.108581.
[32] P. Ropero Giralda, A. Crespo, B. Tagliafierro, C. Altomare, J.M. Domínguez, M. Gómez-Gesteira, G. Viccione, Efficiency and survivability analysis of a point-absorber wave energy converter using DualSPHysics, Renew. Energy 162 (2020) 1763–1776, http://dx.doi.org/10.1016/j.renene.2020.10.012.
[33] B. Tagliafierro, I. Martínez-Estévez, J.M. Domínguez, A.J.C. Crespo, M. Göteman, J. Engström, M. Gómez-Gesteira, A numerical study of a taut-moored point-absorber wave energy converter with a linear power take-off system under extreme wave conditions, Appl. Energy 311 (2022) 118629, http://dx.doi.org/10.1016/j.apenergy.2022.118629.
[34] H. Wendland, Piecewise polynomial, positive definite and compactly supported radial functions of minimal degree, Adv. Comput. Math. 4 (1995) 389–396, http://dx.doi.org/10.1007/BF02123482.

[35] E.Y.M. Lo, S. Shao, Simulation of near-shore solitary wave mechanics by an incompressible SPH method, Appl. Ocean Res. 24 (2002) 275–286, http://dx.doi.org/10.1016/S0141-1187(03)00002-6.
[36] R.A. Dalrymple, B.D. Rogers, Numerical modeling of water waves with the SPH method, Coast. Eng. 53 (2006) 141–147, http://dx.doi.org/10.1016/j.coastaleng.2005.10.004.
[37] G. Fourtakas, J.M. Dominguez, R. Vacondio, B.D. Rogers, Local uniform stencil (LUST) boundary condition for arbitrary 3-D boundaries in parallel smoothed particle hydrodynamics (SPH) models, Comput. Fluids 190 (2019) 346–361, http://dx.doi.org/10.1016/j.compfluid.2019.06.009.
[38] D. Molteni, A. Colagrossi, A simple procedure to improve the pressure evaluation in hydrodynamic context using the SPH, Comput. Phys. Commun. 180 (2009) 861–872, http://dx.doi.org/10.1016/j.cpc.2008.12.004.
[39] M. Antuono, A. Colagrossi, S. Marrone, Numerical diffusive terms in weakly-compressible SPH schemes, Comput. Phys. Commun. 183 (2012) 2570–2580, http://dx.doi.org/10.1016/j.cpc.2012.07.006.
[40] A. English, J.M. Domínguez, R. Vacondio, A.J.C. Crespo, P.K. Stansby, S.J. Lind, L. Chiapponi, M. Gómez-Gesteira, Modified dynamic boundary conditions (mDBC) for general-purpose smoothed particle hydrodynamics (SPH): application to tank sloshing, dam break and fish pass problems, Comput. Part. Mech. 9 (2022) 911–925, http://dx.doi.org/10.1007/s40571-021-00403-3.
[41] A.J. Crespo, M. Gómez-Gesteira, R.A. Dalrymple, Boundary conditions generated by dynamic particles in SPH methods, Comput., Mater. Continua. 5 (2007) 173–184.
[42] R.A. Dalrymple, O. Knio, SPH Modelling of Water Waves, (2012) 779–787. http://dx.doi.org/10.1061/40566(260)80.
[43] S. Marrone, M. Antuono, A. Colagrossi, G. Colicchio, D. Le Touzé, G. Graziani, δ-SPH model for simulating violent impact flows, Comput. Methods Appl. Mech. Eng. 200 (2011) 1526–1542, http://dx.doi.org/10.1016/j.cma.2010.12.016.
[44] M.B. Liu, G.R. Liu, Restoring particle consistency in smoothed particle hydrodynamics, Appl. Numer. Math. 56 (2006) 19–36, http://dx.doi.org/10.1016/j.apnum.2005.02.012.
[45] R.B. Canelas, J.M. Domínguez, A.J.C. Crespo, M. Gómez-Gesteira, R.M.L. Ferreira, A Smooth Particle Hydrodynamics discretization for the modelling of free surface flows and rigid body dynamics, Int. J. Numer. Methods Fluids 78 (2015) 581–593, http://dx.doi.org/10.1002/fld.4031.
[46] B. Leimkuhler, C. Matthews, Introduction, in: B. Leimkuhler, C. Matthews (Eds.), Molecular Dynamics: With Deterministic and Stochastic Numerical Methods, Springer International Publishing, Cham, 2015, pp. 1–51, http://dx.doi.org/10.1007/978-3-319-16375-8_1.
[47] A.N. Parshikov, S.A. Medin, I.I. Loukashenko, V.A. Milekhin, Improvements in SPH method by means of interparticle contact algorithm and analysis of perforation tests at moderate projectile velocities, Int. J. Impact Eng. 24 (2000) 779–796, http://dx.doi.org/10.1016/S0734-743X(99)00168-2.
[48] J.J. Monaghan, A. Kos, Solitary waves on a cretan beach, J. Waterw., Port, Coast., Ocean Eng. 125 (1999) 145–155, http://dx.doi.org/10.1061/(ASCE)0733-950X(1999)125:3(145).
[49] T. Belytschko, L.W. Glaum, Applications of higher order corotational stretch theories to nonlinear finite element analysis, Comput. Struct. 10 (1979) 175–182, http://dx.doi.org/10.1016/0045-7949(79)90085-3.
[50] C.A. Felippa, B. Haugen, A unified formulation of small-strain corotational finite elements: I, Theory, Comput. Methods Appl. Mech. Eng. 194 (2005) 2285–2335, http://dx.doi.org/10.1016/j.cma.2004.07.035.
[51] C.C. Rankin, B. Nour-Omid, The use of projectors to improve finite element performance, Comput. Struct. 30 (1988) 257–267, http://dx.doi.org/10.1016/0045-7949(88)90231-3.
[52] A. Tasora, P. Masarati, Analysis of rotating systems using general-purpose multibody dynamics, in: P. Pennacchi (Ed.), Proceedings of the 9th IFToMM International Conference on Rotor Dynamics, Springer International Publishing, Cham, 2015, pp. 1689–1701, http://dx.doi.org/10.1007/978-3-319-06590-8_139.
[53] M.A. Crisfield, U. Galvanetto, G. Jelenić, Dynamics of 3-D co-rotational beams, Comput. Mech. 20 (1997) 507–519, http://dx.doi.org/10.1007/s004660050271.
[54] O.A. Bauchau, J.I. Craig, Euler–Bernoulli beam theory, in: O.A. Bauchau, J.I. Craig (Eds.), Structural Analysis, Springer Netherlands, Dordrecht, 2009, pp. 173–221, http://dx.doi.org/10.1007/978-90-481-2516-6_5.
[55] J.M. Gere, S.P. Timoshenko, Mechanics of Materials, Springer US, Boston, MA, 1991.
[56] H.M. Hilber, T.J.R. Hughes, R.L. Taylor, Improved numerical dissipation for time integration algorithms in structural dynamics, Earthq. Eng. Struct. Dyn. 5 (1977) 283–292, http://dx.doi.org/10.1002/eqe.4290050306.
[57] N.M. Newmark, A method of computation for structural dynamics, Trans. Am. Soc. Civ. Eng. 127 (1962) 1406–1433, http://dx.doi.org/10.1061/TACEAT.0008448.
[58] D. Negrut, R. Rampalli, G. Ottarsson, A. Sajdak, On an implementation of the hilber-hughes-taylor method in the context of index 3 differential-algebraic equations of multibody dynamics (DETC2005-85096), J. Comput. Nonlinear Dyn. 2 (2006) 73–85, http://dx.doi.org/10.1115/1.2389231.
[59] L.D. Landau, E.M. Lifshitz, Theory of Elasticity: Volume 7, Pergamon Press, 1970.
[60] S. Timoshenko, S. Woinowsky-Krieger, Theory of Plates and Shells, McGraw-hill, New York, 1959.
[61] G. Fourey, Développement D'Une Méthode de Couplage Fluide Structure SPH Eléments Finis En Vue de Son Application à L'Hydrodynamique Navale (Ph.D.thesis), Ecole Centrale de Nantes, 2012.
[62] F. Xie, W. Zhao, D. Wan, MPS-DEM coupling method for interaction between fluid and thin elastic structures, Ocean Eng. 236 (2021) 109449, http://dx.doi.org/10.1016/j.oceaneng.2021.109449.
[63] C. Antoci, M. Gallati, S. Sibilla, Numerical simulation of fluid–structure interaction by SPH, Comput. Struct. 85 (2007) 879–890, http://dx.doi.org/10.1016/j.compstruc.2007.01.002.
[64] M.-J. Li, Y. Lian, X. Zhang, An immersed finite element material point (IFEMP) method for free surface fluid–structure interaction problems, Comput. Methods Appl. Mech. Eng. 393 (2022) 114809, http://dx.doi.org/10.1016/j.cma.2022.114809.

[65] Z.-F. Meng, A.-M. Zhang, J.-L. Yan, P.-P. Wang, A. Khayyer, A hydroelastic fluid–structure interaction solver based on the Riemann-SPH method, Comput. Methods Appl. Mech. Eng. 390 (2022) 114522, http://dx.doi.org/10.1016/j.cma.2021.114522.

[66] C. Antoci, Simulazione Numerica Dell'Interazione Fluido-Struttura Con la Tecnica SPH, Vol. 100 (Ph.D. thesis), Universita di Pavia, 2006, Ph. D. thesis.

[67] M. McLoone, N.J. Quinlan, Coupling of the meshless finite volume particle method and the finite element method for fluid–structure interaction with thin elastic structures, Eur. J. Mech. B/Fluids 92 (2022) 117–131, http://dx.doi.org/10.1016/j.euromechflu.2021.12.001.

[68] G. Zhang, W. Zhao, D. Wan, Partitioned MPS-FEM method for free-surface flows interacting with deformable structures, Appl. Ocean Res. 114 (2021) 102775, http://dx.doi.org/10.1016/j.apor.2021.102775.

[69] K. Liao, C. Hu, M. Sueyoshi, Free surface flow impacting on an elastic structure: Experiment versus numerical simulation, Appl. Ocean Res. 50 (2015) 192–208, http://dx.doi.org/10.1016/j.apor.2015.02.002.

[70] A. Khayyer, N. Tsuruta, Y. Shimizu, H. Gotoh, Multi-resolution MPS for incompressible fluid-elastic structure interactions in ocean engineering, Appl. Ocean Res. 82 (2019) 397–414, http://dx.doi.org/10.1016/j.apor.2018.10.020.